NTNU
Innovation and Creativity

Estimation of Resrvoir Properties by Joint Inversion of Seismic AVO and CSEM data

Andreas Holm

Master of Science in Physics and Mathematics
Submission date: July 2007
Supervisor: Jo Eidsvik, MATH

Norwegian University of Science and Technology
Department of Mathematical Sciences

Problem Description

-Create a statistical model for inversion of CSEM and seismic AVO data

-Develop a method for approximating the posterior distribution of the two reservoir parameters saturation and porosity.

-Develop a method for estimating the noise levels in the data.

-Test the model on both synthetic and real data.

Assignment given: 08. February 2007
Supervisor: Jo Eidsvik, MATH

Abstract

Porosity and water saturation in a horizontal top-reservoir are estimated from seismic AVO (Amplitude Versus Offset) data and Controlled Source Electromagnetic (CSEM) data jointly. A model connecting porosity and saturation to both AVO effects and to the phase shift of electromagnetic signals is constructed. In this model, Gassmann's equations, Archie's law, Zoeppritz' equations and ray-tracing is involved. We use a Bayesian approach to solve the inversion problem, and the solution is given as posterior distributions for the parameters of interest. We also investigate the noise levels in the two types of data, and how these affect the estimates of the reservoir properties. Gaussian assumptions and linearizations are made to ensure analytically tractable posterior distributions for porosity and saturation, and a Gibbs sampler is used to explore the joint posterior for porosity, saturation and noise levels. The method is applied to both synthetic data, and field data from the Troll gas field. The results from the joint inversion are compared to results from using seismic data exclusively and a clear improvement is found in the estimates of the synthetic case. The results from the Troll data are more ambiguous, probably caused by the problem of picking seismic data along the top-reservoir and inaccuracies in the fixed parameters in the geophysical forward model.

Preface

The work with this Diploma thesis has been carried out from February to July 2007 at the Norwegian University of Science and Technology (NTNU), Department of Mathematical Sciences. Its submission marks the end of my six years as a student at NTNU, as it is the final step on the way to achieving the Master of Technology degree.

First and foremost I would like to thank my supervisor Jo Eidsvik for his invaluable help and guidance throughout the process of completing this report. I would also like to thank Ketil Hokstad and Terje Tollefsen at Statoil, for providing me with the data necessary to apply the method developed in this thesis on a real life scenario. Lastly i would like to thank my co-students for interesting lunch-discussions, diversions when I needed a break and numerous ping-pong matches.

Andreas Holm, Trondheim 06.07.2007

Contents

1 Introduction

When performing a geophysical survey with hydrocarbon exploration in mind, the two most crucial properties to estimate are the porosity ϕ and the water saturation s_w. The porosity is important as it tells us the the amount of fluid in the rock, and the water saturation tells us what this fluid consists of, as the hydrocarbon saturation equals $1 - s_w$. Unfortunately there is currently no method for measuring these properties directly, and the relation between what we can measure and what we are interested in is in most cases far from obvious.

Except for drilling wells, seismic gathers have until recently been the only alternative in geophysical exploration. In a situation with a horizontally layered exploration area, a seismic gather can after processing give information about the reflection coefficients between the different layers, and also how the amplitude of the seismic signal varies with the distance between source and receiver, the so-called Amplitude Versus Offset(AVO)-gradient. To obtain the reflection coefficient and the AVO-gradient it is necessary to process the data from the seismic gather. This involves removing of the direct wave, guided wave and multiples, common midpoint gathers and stacking. Picking the signal which is reflected from the transition between cap-rock and anomaly and disregarding all other signals is also part of the pre-processing. The pre-processing is a complex procedure entailed with a lot of uncertainty, and it can therefore introduce systematic error in the data. This is unfortunate, but difficult to avoid. Both the reflection coefficient and the AVO gradient are determined by the rock's elastic parameters. An elastic and isotropic rock is fully described by three different elastic parameters. The three most commonly used are p-wave velocity, s-wave velocity and density. Gassmann's equation [16] relates the elastic parameters to s_w and ϕ, but the dependency on s_w is weak, and even for very low noise levels most of the information about s_w is lost in a seismic gather.

A property that is highly dependent on s_w, however, is the electrical conductivity. Conductivity and water saturation are related through Archie's law [3], and the conductivity can be measured by performing a Controlled Source Electromagnetic Signal(CSEM) gather. CSEM gathers are a relatively new addition to the geophysicists toolbox, and are still very much a developing technology, even though it has already been used for commercial purposes. Its strength lies in the ability to gather information not obtainable by traditional seismic investigations, though the accuracy of this information is low compared to seismics. The EM-signals emitted during a CSEM-gather has a very low frequency, usually in the range of $0.25Hz - 2Hz$. This means that the wavelengths are large, and our image of the subsurface will be fairly coarse compared to seismics, where the frequency typically is around $40Hz$. A combination of these two techniques would therefore seem like the natural next step in geophysical exploration, and attempts og this have already been made ([13],[12]). Until now the focus has, however, been on layered models with uniform layers, i.e only variation along the vertical axis. In this paper we will concentrate on a model with uniform overburden, but an anomaly where both saturation and porosity varies within the same layer. This is a more suitable approach for exploring a large area as it is not confined to one single spot.

Combining the information from both a seismic and a CSEM gather enables us to

achieve more accurate estimates of the rock-properties than we would get from any one of them alone. We will run a comparison between our results and estimates obtained from using seismic exclusively, to see how large the improvement actually is. Performing a CSEM gather is expensive, and it is therefore important that the relative size of the improvement is large enough to validate the cost associated with further investigations. The calculation of the reservoir properties in the subsurface poses a complex inverse problem, which does not have a deterministic solution due to large amounts of noise and uncertainty. This lack of deterministic solutions validates a statistical approach to the problem, as this enables us not only to find good estimates, but also to quantify the uncertainty of these. In addition to ϕ and s_w, we will also estimate the noise levels in the two different types of data. This is an important aspect of our model, as the result of the inversion is very sensitive to these parameters.

Section 2 introduces the theory behind seismic gathers and the relations needed to link the seismic data to rock properties. In section 3 the same is done for the CSEM gather. In 3.1 we develop the relations needed for linking the CSEM-signals traveltime to the conductivity in the anomaly, while we in 3.2 introduce Archie's law. Section 4 starts by summarizing the complete forward model, i.e. all the physical relations we will utilize in the transition from reservoir properties to measured data. The section is further divided in three parts. In 4.1 we develop the statistical model for s_w and ϕ, and calculate their posterior distribution. In 4.2 we describe a fully Bayesian method including priors for the covariance parameters in the model, and 4.3 gives a brief introduction to Markov Chain Monte Carlo methods and the Gibbs sampler. Section 5 presents the results from running the method. In 5.1 we investigate a synthetic dataset where the true underlying reservoir properties are known, while we in 5.2 use data gathered at the Troll field outside of Bergen. We evaluate the strengths and weaknesses of the inversion method in section 6, both from a theoretical viewpoint, and by considering its performance on the two datasets. We also make suggestions for further improvements on the method.

2 Model for seismic data

When seismic signals are shot into the ground, an echo is created. This echo consists of signals that have been reflected by transitions between different types of layers in the underground. The idea behind using seismic as a tool for geological exploration, is that the amplitude and traveltime of the signal echoed back to the surface is dependent on the properties of the rock through which it has propagated. An off-shore seismic gather is performed by a boat towing one or more cables with multiple hydrophones attached to them. At regular time intervals a seismic signal is emitted, and the hydrophones register the resulting echo. Since all areas of the subsurface are hit by seismic signals several times during the gather, we get the opportunity to investigate the relation between the amplitude of the echo and the distance between source and receiver, so called AVO analysis.

When the offset increases, the amplitude of the received signal usually decreases, due to the geometrical spreading and attenuation, but for reflections from hydrocarbon saturated rocks we have the opposite effetct, and the amplitude increases with offset [16]. So the AVO-relation contains a lot of information about the rock properties in the sub-surface, and it is actually one of the key components in seismic investigations. The preprocessing of seismic data is a well explored subject, and a more thorough study can be found in for example [16] or [4]. In the following we focus on reflections at top-reservoir. These data are usually obtained by careful picking from a stack of offset gathers, and play a crucial role in reservoir characterization and for drilling purposes. Here we will suffice to say that by utilizing both AVO characteristics and traveltimes it is possible to find the zero-offset reflection coefficients R_{PP} from the reflection between the cap-rock and the anomaly plus the corresponding AVO-gradients G_{AVO}.

Since our ultimate goal is to achieve an estimate of the porosity and water-saturation in the anomaly, it is crucial to find a reliable connection between these parameters and the data acquired from the seismic gather. Unfortunately this relation is not straightforward, and obtaining it necessitates utilizing some empirical relations and assumptions, as well as an intermediate step calculating the elastic parameters. From Aki and Richards' simplification of the Zoeppritz equations [1], we have the relations

$$R_{PP} = \frac{\rho_A V_{PA} - \rho_C V_{PC}}{\rho_A V_{PA} + \rho_C V_{PC}} \tag{2.1}$$

$$G_{AVO} = \frac{\Delta V_P}{2V_P} - 2\frac{V_S^2}{V_P^2}\left\{\frac{\Delta\rho}{\rho} + 2\frac{\Delta V_S}{V_S}\right\} \tag{2.2}$$

where

$$
\begin{aligned}
V_{PC}, V_{PA}, V_{SC}, V_{SA} &= \text{P- and S-wave velocities in cap-rock(c) and anomaly(a)} \\
\rho_C, \rho_A &= \text{Density in cap-rock(c) and anomaly(a)} \\
\Delta V_P &= V_{PA} - V_{PC} \\
\Delta V_S &= V_{SA} - V_{SC} \\
\Delta\rho &= \rho_A - \rho_C \\
V_P &= \frac{V_{PA} + V_{PC}}{2} \\
V_S &= \frac{V_{SA} + V_{SC}}{2} \\
\rho &= \frac{\rho_A + \rho_C}{2}.
\end{aligned}
$$

Thus a forward-model going from density and wave-velocities to R_{PP} and G_{AVO} has been established. This relation is derived from the wave-equation, and is therefore fairly accurate under ideal conditions. From V_P, V_S and ρ we can find two different elastic parameters, the bulk-modulus K and the shear-modulus G using the following transformations

$$K = \rho\left(V_P^2 - \frac{4}{3}V_S^2\right) \tag{2.3}$$

$$G = \rho V_S^2. \tag{2.4}$$

The only reason for performing this transformation is that K and G will be more suitable than wave velocities when describing the transition from ϕ and s_w to elastic parameters. Note that working with (ρ, G_{AVO}, K) instead of (ρ, V_p, V_S) is nothing more than a reparameterization of the three dimensional space of elastic constants. The relations between (s_w, ϕ) and the elastic constants are still not well understood theoretically, and to a large degree it will be necessary to rely on empirical relations derived from well-logs. Cross-plotting measurements of ϕ with K and G shows that these can be approximated by a linear function of ϕ. We will rely on a linear relation in this work, but it is worth noting that the amount of noise in such cross-plots is considerable, and other relations than linearity have been suggested, see for example [5].

As seen from equation 2.4, the shear-modulus depends only on V_S and ρ. Since shear-waves are unable to propagate through both water and gas alike, G will be virtually independent of variations in s_w. This means that when G is known, ϕ can easily be calculated to within the precision of the linear relation found from cross-plotting. The bulk-modulus on the other hand is highly dependent of both ϕ and s_w, and to get an estimate of s_w we will have to make use of the Gassmann equation. This equation relates the bulk-modulus for different levels of water saturation, and can be written down in numerous forms, the following is from [16]

$$\frac{K_{sat}}{K_0 - K_{sat}} = \frac{K_{dry}}{K_0 - K_{dry}} + \frac{K_{fl}}{\phi(K_0 - K_{fl})} \tag{2.5}$$

where

K_{dry} = Bulk modulus of dry rock.
K_{sat} = Bulk modulus of the rock with pore fluid.
K_0 = Bulk modulus of mineral material making up rock. Tabelized value for quartz.
K_{fl} = Bulk modulus of pore fluid. Tabelized values for water and gas

Since K_{dry} and K_0 both are independent of the saturation, we have for all levels of saturation

$$\frac{K_{sat}}{K_0 - K_{sat}} - \frac{K_{fl}}{\phi(K_0 - K_{fl})} = C \tag{2.6}$$

where C is a constant. The bulk modulus for two different saturation levels in the same rock type are thus related as

$$\frac{K_{sat1}}{K_0 - K_{sat1}} - \frac{K_{fl1}}{\phi(K_0 - K_{fl1})} = \frac{K_{sat2}}{K_0 - K_{sat2}} - \frac{K_{fl2}}{\phi(K_0 - K_{fl2})}. \tag{2.7}$$

From well logs we can obtain the bulk modulus for given saturation and porosity values. Since K_0 is known, this enables us to calculate one side of equation 2.7. On the other side we now have two unknowns, K_{sat2} and K_{fl2}, which both depend on the water saturation s_{w2}. Assuming that the rock is only filled with water and gas, K_{fl2} can easily be calculated as

$$\frac{1}{K_{fl2}} = \frac{s_{w2}}{K_{water}} + \frac{1 - s_{w2}}{K_{gas}}. \tag{2.8}$$

The bulk modulus of water and gas are known values and we now have the following expression for K_{sat2}

$$\begin{aligned} \frac{K_{sat2}}{K_0 - K_{sat2}} &= \frac{K_{sat1}}{K_0 - K_{sat1}} - \frac{K_{fl1}}{\phi(K_0 - K_{fl1})} + \frac{K_{fl2}}{\phi(K_0 - K_{fl2})} \\ \frac{K_{sat2}}{K_0 - K_{sat2}} &= A \\ K_{sat2} &= \frac{AK_0}{1 + A}. \end{aligned} \tag{2.9}$$

Figure 2.1 illustrates the relationship between the shear and bulk modulus and the porosity. The multiple lines in the bulk modulus plot signifies different levels of water saturation. A given value of the bulk modulus can thus represent a number of different combinations of saturation and porosity. Since water is less compressible than gas, the bulk modulus will increase with water saturation. The shear modulus on the other hand, is only dependent on the porosity. The relation is linear and the porosity can therefore easily be calculated when the shear modulus is given. Utilizing this porosity together with the bulk modulus enables us to get an estimate of the saturation.

The last equation needed to complete our seismic forward-model is one relating ϕ and s_w to ρ. As both the density of water, gas and the reservoir rock are already known this is readily identified as

$$\rho = \rho_0(1 - \phi) + \rho_w \phi s_w + \rho_g \phi(1 - s_w) \tag{2.10}$$

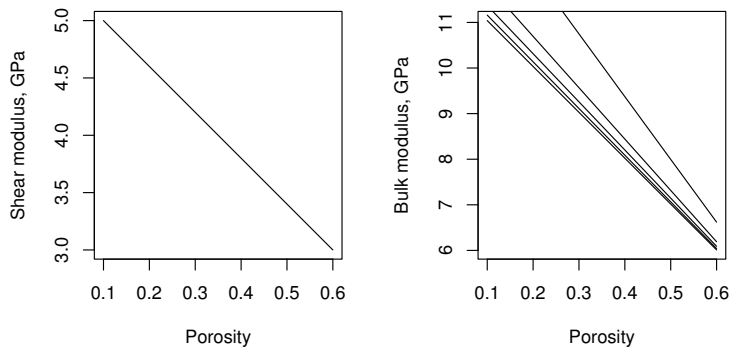

Figure 2.1: Bulk and shear modulus plotted as a function of porosity. The different lines in the bulk modulus plot illustrates how different water saturation levels causes a shift in the relation between bulk modulus and porosity, while shear modulus is unaffected by watersaturation. The saturation levels are (0.9, 0.7, 0.5, 0.3, 0.1) from top to bottom.

where ρ_0, ρ_w and ρ_g denotes the densities of rock, water and gas respectively. For a given pair of porosity and saturation, we are now able to compute ρ and the elastic parameters of the fluid-saturated rock using both the Gassmann equation and our empirical relation. We can then proceed from these to calculate the zero-offset reflection coefficient and the AVO-gradient as shown in equations 2.1 and 2.2. We define f_1 as the function going from the space of saturation and porosity and into the space of seismic readings.

$$(s_w, \phi) \xrightarrow{f_1} (R_{PP}, G_{AVO}) \tag{2.11}$$

3 Model for CSEM data

Though the idea of using controlled source electromagnetic (CSEM) signals to investigate conductivity properties below the sea floor has been around for some time [7], the practical challenges involved have been substantial, and the first survey actually utilizing this method was performed in 2002 offshore Angola [9]. The procedure used in this survey is called sea bed logging (SBL), and it has later become the standard technique for collecting CSEM data, up to the point where the terms CSEM and SBL now are being used interchangeably. An SBL survey is performed as illustrated in figure 3.1. An electric dipole is being towed close to the sea floor. On the sea floor multiple receivers have been deployed, and these record the electromagnetic signal after it has travelled through the anomaly. The received signal will be highly dependent on the conductivity in seawater, overburden and anomaly, ϑ_w, ϑ_o and ϑ respectively.

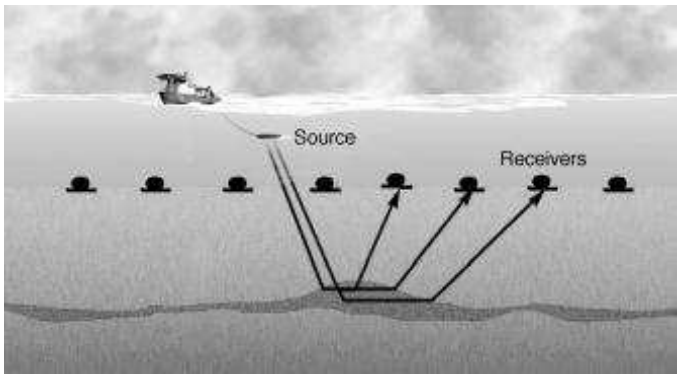

Figure 3.1: Illustration of a typical sea bed logging setup. The electric dipole emits EM-signals that travel through the overburden and along the anomaly before they are reflected up to the seabed situated receivers. The image is taken from [2]

The propagation of low-frequent EM-signals can be described both as a wave- and a diffusion process. A thorough discussion of this can be found in [15]. We will be working with low-frequent signals registered at great distance from the source, and in this situation the diffusion approximation will be most suitable. For EM-signals in a homogenous, non-magnetic medium, we have the relation

$$\nabla^2\psi = k^2\psi \tag{3.1}$$

where ψ is a scalar potential function. Equation (3.1) has the solution

$$\psi = e^{k\cdot r} \tag{3.2}$$

where

$$k^2 = i\mu_0\omega(\vartheta + i\omega\epsilon). \tag{3.3}$$

Here k represents the wave-vector, r the position-vector, μ_0 magnetic permeability in vacuum, ϵ permitivity, ϑ conductivity and ω angular frequency. Since we are considering

low-frequency signals in media with high conductivity $\vartheta \gg \omega\epsilon$. Neglecting the term $\omega\epsilon$ in equation 3.3 gives us

$$k = \pm(1+i)\sqrt{\frac{\mu_0\vartheta\omega}{2}}. \tag{3.4}$$

We can now apply the eikonal equation (see [17],[19]) to find the phase difference τ between source and receiver.

$$\tau = \int_r \sqrt{\mu_0\vartheta(x)}dx \tag{3.5}$$

where the integration is along the path of an EM-signal from source to receiver. As can be seen from equation (3.5), the phase difference τ is dependent on both the conductivity and the ray-path. This implies that calculations of ray-paths, so-called ray-tracing, combined with the inversion of phase-data can give valuable information about the conductivity in the media travelled by the EM-signal.

Figure 3.2 shows synthetic data for τ generated by solving the eikonal-equation. This is a fairly complicated and time-consuming process, which has to be performed for every source/receiver pair. It is however worth noting that when the offset, i.e. the distance between source and receiver, becomes large, the phase is approximately a linear function of offset. From equation (3.5) we know that the slope of this function must be $\sqrt{\mu_0\vartheta}$. We can therefore get an estimate of the conductivity by simply plotting phase against offset and measuring the slope. Unfortunately this will only give us a mean value of all the different levels of conductivity in the anomaly. To be able to discern these levels a ray-tracing routine will have to be performed.

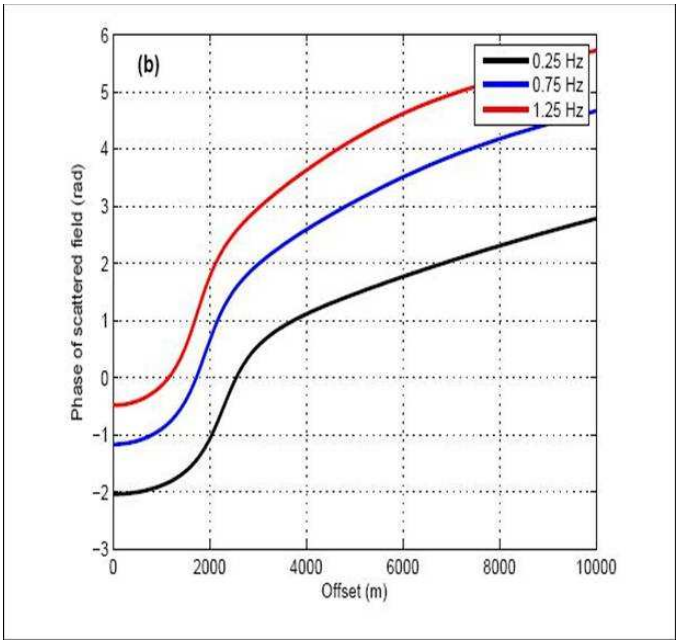

Figure 3.2: Synthetic phase data generated with basis in the conditions at the Troll gas field. The figure is from [18]

3.1 Traveltime calculations

In geophysics the term traveltime is usually employed in the context of seismic waves, and then it refers to the actual amount of time that passes from the signal is emitted until it reaches the receiver. When working with EM-signals however, we are no longer measuring time, but the phase-shift of the signal which is denominated $|\sqrt{sec}|$. Likewise the CSEM-signal's velocity is actually a pseudo velocity with denomination $|\frac{m}{\sqrt{sec}}|$. Even though this nomenclature, developed for seismics, does not give a stringently correct description of the physics involved, the analogy with velocity and time makes the model intuitively easier to understand. It is also sufficiently accurate for our purposes, and we have therefore chosen to use it.

We will be concentrating on the refraction wave, or so-called guided-wave, as illustrated in Figure 3.3. This is the signal that enters the anomaly at the critical angle of incidence, travels horizontally along the anomaly and then up to the receiver. The total distance travelled can be expressed as

$$d_{total} = d_w + 2d_o + l \tag{3.6}$$

$$= \frac{d_0}{\cos\theta_0} + 2\frac{d_1}{\cos\theta_1} + l. \tag{3.7}$$

d_w, d_0 and l is the distance travelled through water, overburden and anomaly respectively. Throughout this thesis we will assume that the signal exits the anomaly at the same angle as it entered, hence the 2 in front of d_o. From Snell's law we know that the different angles of incidence and pseudo-velocities are related as

$$\frac{\sin\theta_0}{v_0} = \frac{\sin\theta_1}{v_1} = \frac{\sin\theta_2}{v_2} = p \tag{3.8}$$

where v_i for $i = 0, 1, 2$ represent the pseudo-velocities in the three layers. For the refraction wave we know that $\theta_2 = 90^o$ since it travels horizontally in the anomaly. By using the relation

$$\cos\theta_i = \sqrt{1 - \sin\theta_i^{\,2}} = \sqrt{1 - v_i^2 p^2} \tag{3.9}$$

for $i = 0, 1$, we can transform equation 3.7 into

$$d_{total} = \frac{d_0}{\sqrt{1 - v_0^2 p^2}} + 2\frac{d_1}{\sqrt{1 - v_1^2 p^2}} + l. \tag{3.10}$$

The total traveltime will then be

$$\tau = \frac{d_0}{v_0\sqrt{1 - v_0^2 p^2}} + 2\frac{d_1}{v_1\sqrt{1 - v_1^2 p^2}} + \frac{l}{v_2}. \tag{3.11}$$

From equation 3.5 we know that τ also equals $\sqrt{\mu_0\vartheta}$ integrated along the ray-path, hence

$$v_i = (\sqrt{\mu_0\vartheta_i})^{-1}. \tag{3.12}$$

Combining equation 3.12 with equation 3.11 provides the necessary link between the conductivity ϑ and the traveltime τ.

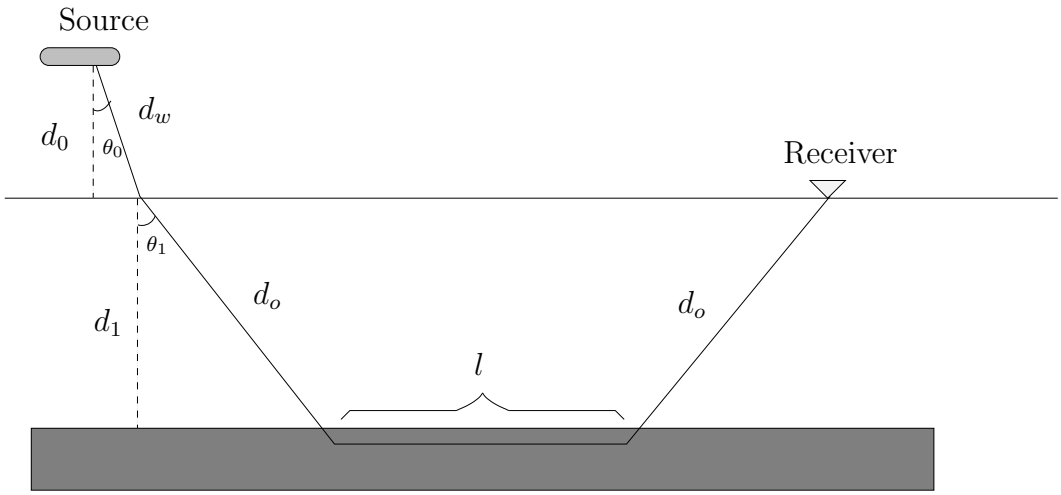

Figure 3.3: The measured EM-signal is emitted at an angle θ_0. It travels a distance d_w through the water before it is refracted at the ocean floor. It proceeds to travel through the overburden for a distance d_o before it encounters the anomaly. θ_1 is the critical angle of incidence, and the signal will therefore move horizontally in the overburden, until it is refracted up through the overburden and reaches the receiver.

3.2 Archie's law

As with the seismic data, we will have to establish a connection between the observed CSEM-data and the parameters we wish to estimate, ϕ and s_w. The transition from conductivity to ϕ and s_w is found by utilizing Archies law, which is purely empirical, but often found to be quite accurate [3]. Archies law is stated as follows

$$\vartheta = C s_w^{\alpha} \phi^{\beta}. \tag{3.13}$$

α and β are often referred to as the saturation exponent and the porosity exponent. Both these and the constant C can be calculated from well logs where both s_w, ϕ and ϑ have been measured. This can be done by using ordinary linear regression on the logarithmic-values. Figure 3.4 shows how Archie's law relates conductivity with saturation and porosity when $C = 1.28, \alpha = 1.31$ and $\beta = 0.14$. In the left plot the saturation is fixed at $0.2, 0.5$ and 0.8, and in the right plot the porosity is fixed at $0.2, 0.35$ and 0.55. It is clear from this Figure that variations in conductivity mainly is caused by different levels of saturation.

This completes our CSEM forward model and we now define f_2 as the function going from the space of saturation and porosity into the space of traveltimes.

$$(s_w, \phi) \xrightarrow{f_2} \tau \tag{3.14}$$

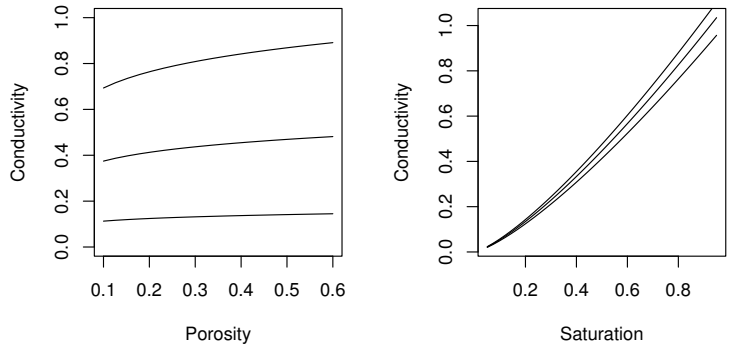

Figure 3.4: Conductivity cross-plotted with porosity and saturation using Archie's law. In the left plot $s_w = (0.2, 0.5, 0.8)$ and in the right plot $\phi = (0.2, 0.35, 0.55)$. $C = 1.28, \alpha = 1.33$ and $\beta = 0.14$ in both plots. It is clear from these plots that the conductivity is more sensitive to changes in saturation than changes in porosity.

4 Statistical framework

By combining the relations developed in section 2 and 3 we have a fully developed forward model for both seismic and CSEM data, as illustrated in Figure 4.1. Since we are measuring two very different physical properties, we also focus on different aspects of the subsurface when modelling. This is illustrated in Figure 4.2. For the seismic gather it is only the elastic properties of the cap-rock layer directly above the anomaly that are of interest, while for the CSEM gather the conductivity of the entire overburden and the seawater strongly affects the measurement. All these parameters are assumed known in our model. To solve the inversion problem of estimating ϕ and s_w based on seismic and CSEM data we have chosen to use a Bayesian approach. This means that we view the parameters we wish to estimate as realizations of stochastic variables with a given distribution. Our aim is thus to calculate these distributions, and to give confidence bounds on the parameters of interest.

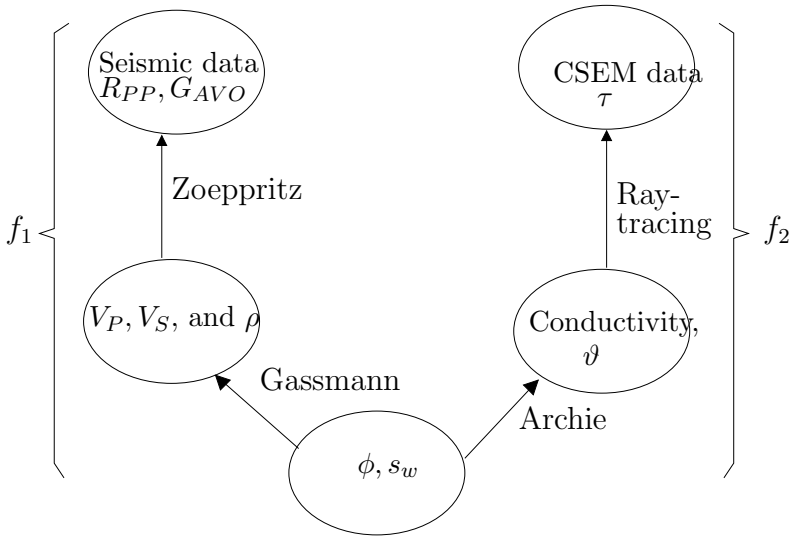

Figure 4.1: Forward model. The figure illustrates which relations are being used to go from the parameters of interest to the observed data.

4.1 Model for saturation and porosity

In order to make our model analytically tractable it is desirable to have a Gaussian prior distribution. Since ϕ and s_w both have an upper and lower limit they cannot be directly modeled as Gaussian variables, and it is therefore necessary to perform a transformation of these variables. We define

$$m_\phi = \log \frac{\phi - \phi_{max}}{\phi_{min} - \phi} \tag{4.1}$$

$$m_{s_w} = \log \frac{s_w - s_{w,max}}{s_{w,min} - s_w} \tag{4.2}$$

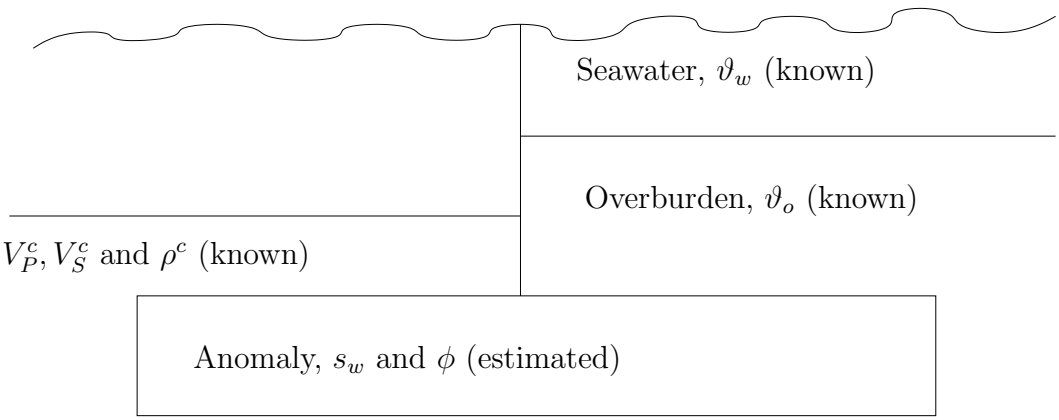

Figure 4.2: Inversion domain for seismics on the left and for CSEM on the right

with inverse functions

$$\phi(m_\phi) = \frac{e^{m_\phi}\phi_{max} + \phi_{min}}{1 + e^{m_\phi}} \tag{4.3}$$

$$s_w(m_{s_w}) = \frac{e^{m_s}s_{w,max} + s_{w,min}}{1 + e^{m_s}} \tag{4.4}$$

where $s_{w,min}, s_{w,max}, \phi_{min}$ and ϕ_{max} must be tuned in the context of an application. We obviously have $0 \leq s_{w,min}, \phi_{min}$ and $s_{w,max}, \phi_{max} \leq 1$, but prior information about the subsurface may enable us to decrease the intervals. These transformed variables are called the logit values of the porosity and saturation, and their support is the entire real line. Hence they can be modeled as realizations from a Gaussian distribution. Let m be a vector containing logit values for all our target parameters. If we divide the anomaly into p sections, each with a different porosity and saturation, m will be a vector of length $2p$.

$$m = (m_{s_w,1}, m_{\phi,1}, m_{s_w,2}, \ldots, m_{s_w,p}, m_{\phi,p}) \tag{4.5}$$

where $m_{s_w,i}$ and $m_{\phi,i}$ denote the logit values of the saturation and porosity in the i'th segment of the anomaly. m is now a realization of the stochastic variable M and has the distribution

$$m \sim \pi_M(m) = N(\mu_m, \Sigma_m). \tag{4.6}$$

Let d_S denote the observations from the seismic gather and d_C the observations from the CSEM gather. We denote the length of d_S and d_C with n_{ds} and n_{dc} respectively. Then we construct a vector $d = (d_S, d_C)$ and the values of d will be a function of m plus noise,

$$d = F(m) + \epsilon \qquad \text{where} \qquad \epsilon \sim N(0, T). \tag{4.7}$$

F is the forward model developed in the previous chapters, and consists of the two functions, f_1 which returns the seismic data d_S, and f_2 which returns the CSEM-data d_C. Since both f_1 and f_2 are deterministic functions, the distribution of d conditioned on m is

$$d|m \sim \pi_{D|M}(d) = N(F(m), T). \tag{4.8}$$

ϵ is the noise that explains the discrepancy between the observations and the values calculated from the forward model. This discrepancy arises both from actual noise in the data, and the fact that our forward model does not give an exact description of what happens in reality. Since our model is a simplification, the assumption that $E(\epsilon) = 0$ may not be entirely correct. This is however always the case when working with simplified models, and can only be remedied by describing physical reality exactly, which in turn would be mathematically infeasible. But as long as the random noise dominates the systematic error, the model is sufficiently accurate. The covariance matrix of ϵ, T, will be discussed in closer detail later on in this section.

To find the distribution of m conditioned on d we apply Bayes theorem, which states

$$\pi_{M|D}(m|d) = \frac{\pi_{D|M}(d|m)\pi_M(m)}{\int_S \pi_{D|M}(d|m)\pi_M(m)dm} \tag{4.9}$$

where $S = \mathbb{R}^{2p}$ is the support of M. Since the denominator on the right hand side of equation 4.9 is a constant with respect to m, the kernel of the posterior distribution for $m|d$ lies wholly within the numerator. This means that $\pi_{M|D}(m|d)$ can be analytically calculated as long as $\pi_{D|M}(d|m)$ and $\pi_M(m)$ are conjugate distributions. $\pi_M(m)$ is already chosen to be Gaussian, so it is sufficient too ensure that d can be expressed as a linear combination of the logit varibles m. Unfortunately the forward model developed in the previous sections and equations 4.1 and 4.2 is far from linear with respect to m, so in order to obtain an algebraically convenient posterior distribution it is necessary to use a linearized version of our forward model.

$$\begin{aligned} d &= F(m) + \epsilon \\ &\simeq F(m^*) + \frac{dF}{dm}|_{m^*}(m - m^*) + \epsilon \\ &= \begin{bmatrix} f_1(m^*) \\ f_2(m^*) \end{bmatrix} + \begin{bmatrix} \frac{df_1}{dm} \\ \frac{df_2}{dm} \end{bmatrix}_{m^*} (m - m^*) + \epsilon \\ &= d^* + \epsilon \end{aligned} \tag{4.10}$$

where m^* is a linearization point and d^* consists of values calculated from the linearized forward model. Using d^* instead of $F(m)$ as the expectation of $d|m$ gives us a approximate posterior distribution which has the advantage of being Gaussian. The exponent in this distribution is on the following form

$$\begin{aligned} log\left(\pi_{M|D}(m|d)\right) &\sim log\left(\pi_{D|M}(d|m)\pi_M(m)\right) \\ &\sim -\frac{1}{2}(d - d^*)^T T^{-1}(d - d^*) - \frac{1}{2}(m - \mu)^T \Sigma^{-1}(m - \mu) \\ &= -\frac{1}{2}\left\{d - F(m^*) - \frac{dF}{dm}|_{m^*}(m - m^*)\right\}^T T^{-1}\left\{d - F(m^*) - \frac{dF}{dm}|_{m^*}(m - m^*)\right\} - \\ &\frac{1}{2}(m - \mu)^T \Sigma^{-1}(m - \mu). \end{aligned} \tag{4.11}$$

Ignoring terms independent of m gives us

$$-\frac{1}{2}m^T\left\{\left(\frac{dF}{dm}|_{m^*}\right)^T T^{-1}\frac{dF}{dm}|_{M^*}+\Sigma^{-1}\right\}m$$
$$+m^T\left\{\left(\frac{dF}{dm}|_{m^*}\right)^T T^{-1}(d-F(m^*)+\frac{dF}{dm}|_{m^*}m^*)+\Sigma^{-1}\mu\right\}. \quad (4.12)$$

The mean and variance for the approximate posterior distribution can be calculated as

$$\mu_{m|d}=\left\{\left(\frac{dF}{dm}|_{m^*}\right)^T T^{-1}\frac{dF}{dm}|_{m^*}+\Sigma^{-1}\right\}^{-1}\left\{\left(\frac{dF}{dm}|_{m^*}\right)^T T^{-1}(d-F(m^*)+\frac{dF}{dm}|_{m^*}m^*)+\Sigma^{-1}\mu\right\} \quad (4.13)$$

$$\Sigma_{m|d}=\left\{\left(\frac{dF}{dm}|_{m^*}\right)^T T^{-1}\frac{dF}{dm}|_{m^*}+\Sigma^{-1}\right\}^{-1}. \quad (4.14)$$

From equation 4.13 we see that $\mu_{m|d}$ is highly dependent on m^*. Since the approximate posterior distribution is Gaussian $\mu_{m|d}$ should be the vector with highest probability density, i.e.

$$\arg\max_m \pi_{M|D}(m|d)=\mu_{m|d}. \quad (4.15)$$

Finding this $\mu_{m|d}$ is equivalent to finding the m that maximizes $-\frac{1}{2}(d-F(m))^T T^{-1}(d-F(m))-\frac{1}{2}(m-\mu)^T\Sigma^{-1}(m-\mu)$. This can be done numerically using the following simple iterative algorithm

- Choose a starting point m_o
- Calculate $t_0=-\frac{1}{2}(d-F(m_0)^T T^{-1}(d-F(m_0))-\frac{1}{2}(m_0-\mu)^T\Sigma^{-1}(m_0-\mu)$
- While $\Delta > TOL$
  - set $m_i=\mu_{m|d}$ where $\mu_{m|d}$ is calculated using m_{i-1} and equation 4.13.
  - calculate t_i
  - $\Delta=|t_i-t_{i-1}|$

Δ is a variable measuring how much closer to $\max \pi_{M|D}(m|d)$ the last iteration has brought us. When the progress for a single iteration is smaller than the preset tolerance value TOL, we terminate the process.

4.2 Covariance matrices

Estimation of the covariance matrices Σ and T is an important aspect of this model, which we have yet to deal with. The likelihood covariance matrix T actually consists of two separate matrices one for the seismic data, T_{seis} and one for the CSEM data, T_{CSEM},

and these are assumed to be independent. This is a natural assumption since they are related to different data collection methods. T can consequently be written as

$$T = \begin{bmatrix} T_{seis} & 0 \\ 0 & T_{CSEM} \end{bmatrix}. \tag{4.16}$$

A lot of work have been done on seismic data, and the structure of T_{seis} is therefore relatively well known. We will make use of estimates of T_{seis} found in [8], as this seems to be appropriate for our situation. What is not known however, is the impact of the uncertainty in the seismic data relative to the CSEM data. We will therefore multiply the seismic covariance matrix with a factor σ_S^2, such that

$$T_{seis} = \sigma_S^2 T_S \tag{4.17}$$

where T_S is a block-diagonal matrix consisting of 2×2-matrices on the form

$$\begin{bmatrix} 0.025 & -0.05 \\ -0.05 & 0.0225 \end{bmatrix}, \tag{4.18}$$

giving a correlation coefficient of -0.7 between R_{PP} and G_{AVO}.

When it comes to the CSEM-data the prior knowledge is much more limited. We make the simplified assumption that the noise on the CSEM data is white, and we can write $T_{CSEM} = I\sigma_C^2$. Hence, estimating the likelihood covariance matrix means finding appropriate σ_C^2 and σ_S^2. In accordance with our bayesian line of thought, we start by applying probability distributions to both σ_C^2 and σ_S^2. Since our only prior knowledge about these parameters is that they are positive, an inverse gamma-distribution with a large variance would seem a fitting choice for a prior. When σ_C^2 and σ_S^2 are inverse gamma distributed, σ_C^{-2} and σ_S^{-2} will be gamma distributed. It will be more convenient to work with the inverted variances since they appear naturally in the likelihood expression. Let both σ_C^{-2} and σ_S^{-2} be gamma distributed with parameters (α_C, β_C) and (α_S, β_S), i.e.

$$\begin{aligned} \sigma_C^{-2} &\sim G(\sigma_C^{-2}; \alpha_C, \beta_C) = \frac{1}{\beta_C^{\alpha_C}\Gamma(\alpha_C)}(\sigma_C^{-2})^{\alpha_C - 1} e^{\frac{-\sigma_C^{-2}}{\beta_C}} \\ \sigma_S^{-2} &\sim G(\sigma_S^{-2}; \alpha_S, \beta_S) = \frac{1}{\beta_S^{\alpha_S}\Gamma(\alpha_S)}(\sigma_S^{-2})^{\alpha_S - 1} e^{\frac{-\sigma_S^{-2}}{\beta_S}}. \end{aligned}$$

We can now calculate the posterior distributions for σ_C^{-2} and σ_S^{-2}.

$$\begin{aligned} \pi(\sigma_C^{-2}|d, m, \sigma_S^{-2}) &\propto \pi(d|m, \sigma_S^{-2}, \sigma_C^{-2})\pi(m|\sigma_S^{-2}, \sigma_C^{-2})\pi(\sigma_S^{-2})\pi(\sigma_C^{-2}) \\ &\propto \pi(d|m, \sigma_S^{-2}, \sigma_C^{-2})\pi(\sigma_C^{-2}) \\ &\propto (\sigma_C^{-2})^{\frac{n_{dc}}{2}} e^{\frac{-1}{2}(d_C - f_2(m))^T T_{CSEM}(d_C - f_2(m))} (\sigma_C^{-2})^{\alpha_C - 1} e^{\frac{-\sigma_C^{-2}}{\beta_C}} \\ &= (\sigma_C^{-2})^{\frac{n_{dc}}{2} + \alpha_C - 1} e^{\frac{-1}{2}(d_C - f_2(m))^T \sigma_C^{-2} I (d_C - f_2(m)) + \frac{-\sigma_C^{-2}}{\beta_C}} \\ &= (\sigma_C^{-2})^{\frac{n_{dc}}{2} + \alpha_C - 1} e^{-\sigma_C^{-2}\{\frac{1}{2}(d_C - f_2(m))^T I (d_C - f_2(m)) + \frac{1}{\beta_C}\}}. \end{aligned} \tag{4.19}$$

From equation 4.19 it is clear that the posterior distribution for σ_C^{-2} is the gamma-distribution with parameters

$$\begin{aligned}\alpha_{\sigma_C^{-2}} &= \alpha_C + \frac{n_{dc}}{2} \\ \beta_{\sigma_C^{-2}} &= \left\{\frac{1}{2}(d_C - f_2(m))^T I(d_C - f_2(m)) + \frac{1}{\beta_C}\right\}^{-1}.\end{aligned} \tag{4.20}$$

Similarly $\sigma_S^{-2}|d, m$ will also be gamma-distributed with parameters

$$\begin{aligned}\alpha_{\sigma_S^{-2}} &= \alpha_S + \frac{n_{ds}}{2} \\ \beta_{\sigma_S^{-2}} &= \left\{\frac{1}{2}(d_s - f_1(m))^T T_S^{-1}(d_s - f_1(m)) + \frac{1}{\beta_S}\right\}^{-1}.\end{aligned} \tag{4.21}$$

Since the full conditional distributions are known for both $\sigma_C^{-2}, \sigma_S^{-2}$ and m, we can use a Gibbs sampler to explore the postrior distributions. A Gibbs sampler is a special instance of the Metropolis-Hastings algorithm, which is a Markov Chain Monte Carlo(MCMC) method. More on MCMC-methods in section 4.3.

In our prior distribution of m we assume that saturation and porosity are independent, and that the covariance between the porosity or saturation in two different segments of the anomaly is a decreasing function of distance. We create a Σ that can be written as

$$\Sigma = \sigma_p^2 \Sigma_1 \tag{4.22}$$

where Σ_1 consists of 2×2-matrices on the form

$$\begin{bmatrix} \rho^{|i-j|} & 0 \\ 0 & \rho^{|i-j|} \end{bmatrix}. \tag{4.23}$$

$|i - j|$ is the distance between anomaly segments i and j. We will for most parts of this paper let ρ and σ_P^2 be fixed. We could attempt to estimate these parameters analogous to what we did with σ_C^{-2} and σ_S^{-2}, but from experience we know that letting all parameters be a priori undecided, often causes problems with convergence in the Markov chain used to explore the posterior distribution.

4.3 MCMC methods

According to general Markov chain theory (see for example [10]) every irreducible and ergodic Markov chain will converge to a limit distribution. This distribution is determined by the transition function used to simulate the Markov chain, so the challenge is to create a transition function that makes the markov chain converge to precisely our posterior distribution. One way of doing this is using the Metropolis-Hastings algorithm [11]. A move is proposed by drawing from a proposal distribution $q(x_t, \tilde{x})$. This move is accepted with probability α, where α is defined as

$$\alpha = min\left\{1, \frac{\pi(\tilde{x})q(\tilde{x}, x_t)}{\pi(x_t)q(x_t, \tilde{x})}\right\} \tag{4.24}$$

and $\pi(\cdot)$ is the posterior distribution. If the move is accepted $x_{t+1} = \tilde{x}$, and if it is rejected $x_{t+1} = x_t$. When the full conditional distributions are known, these can be used as proposal distributions, and the acceptance rate α will always be 1. This is what is known as the Gibbs sampler, and is the method we will be using in this paper. The parameters we are trying to estimate are $\sigma_C^{-2}, \sigma_S^{-2}$ and m and their distributions are given in equations 4.13,4.14,4.20 and 4.21. Our sampling algorithm will then become

- for t in 1:L
  - Draw $(\sigma_C^{-2})_t$ from $G(\sigma_C^{-2}|d, m_{t-1})$ as described in section 4.2
  - Draw $(\sigma_S^{-2})_t$ from $G(\sigma_S^{-2}|d, m_{t-1})$ as described in section 4.2
  - Draw m_t from $N\left(\mu_{m|d,(\sigma_C^{-2})_t,(\sigma_S^{-2})_t}, \Sigma_{m|d,(\sigma_C^{-2})_t,(\sigma_S^{-2})_t}\right)$ utilizing the iterative algorithm outlined in section 4.1.
- end

Here L is a large number. After a sufficient burn-in time the Markov chain is run for several iterations to ensure a good approximation of the posterior distribution.

5 Results

In this section we will present results from two different dataset. The first one is synthetic, which means that we have created a model of the subsurface where all parameterts are known, and then used this model to generate data, both with and without noise. The second dataset is compiled of a seismic- and a CSEM gather, that has been performed on the Troll gas field.

5.1 Synthetic data

To investigate the accuracy of our model, we have chosen to apply it on a synthetic case where the true values for porosity and saturation are known. The target horizon is located 1200 meters below the sea floor, and divided into 241 segments of length 100 meters. Each segment i has a unique saturation and porosity, denoted $s_{w,i}$ and ϕ_i. We generate logit values for s_w and ϕ by drawing from a multinormal distribution with expectation zero and covariance matrix Σ_{synt}. The elements of Σ_{synt} are

$$\sigma_{i,j} = \begin{cases} \rho^{\frac{|i-j|}{\xi}} & \text{if both } i \text{ and } j \text{ are even or both are odd} \\ 0 & \text{else} \end{cases} . \tag{5.1}$$

$\rho = 0.9$ and $\xi = 20$. Looking back to equation 4.23 we see that the parameter ξ was not included in our prior model. This means that the generated values will be smoother than we anticipated in our prior distribution. When working with real data the prior assumptions are never exactly correct, and it is therefore interesting, also in the synthetic case, to see how the estimates are affected when the data have not been generated quite as expected.

By inserting the logit values into our forward model, we can calculate reflection coefficients, AVO-gradients and traveltimes for our synthetic case. In Archie's law we use parameters estimated in [6]. These parameters have been found by fitting of log-data collected from well 31/2-1 which is located on the Troll site outside of Bergen. Numerical values for all fixed parameters can be found in table 5.1. Going from left to right, eleven CSEM-receivers have been placed at 7km to 17km with a 1km interval, and CSEM-signals have been emitted with 100m intervals starting 6km left of receiver 1 and ending 6km right of receiver 11. So for every receiver we have traveltime data for offsets ranging from -6km to 6 km. Between receiver 1 and 11 there has also been performed a seismic gather, where the zero-offset reflection coefficient and AVO-gradient has been calculated for every 100m. The situation is illustrated in Figure 5.2.

We have estimated the logit values of s_w and ϕ for two different noise levels in the data generation, for zero noise and for $\sigma_C^2, \sigma_S^2 = 0.3$. The results are plotted in Figures 5.3-5.8. The hyperparameters in the prior distributions for σ_C^2 and σ_S^2 are $\alpha_C, \alpha_S = 0.001$ and $\beta_c, \beta_S = 1000$ in both the synthetic example, and for the Troll data in the next subsection.

In Figure 5.3 we see that for the zero noise data the estimated porosity matches the true values nearly perfect, and the variance in the posterior distribution of ϕ is close to

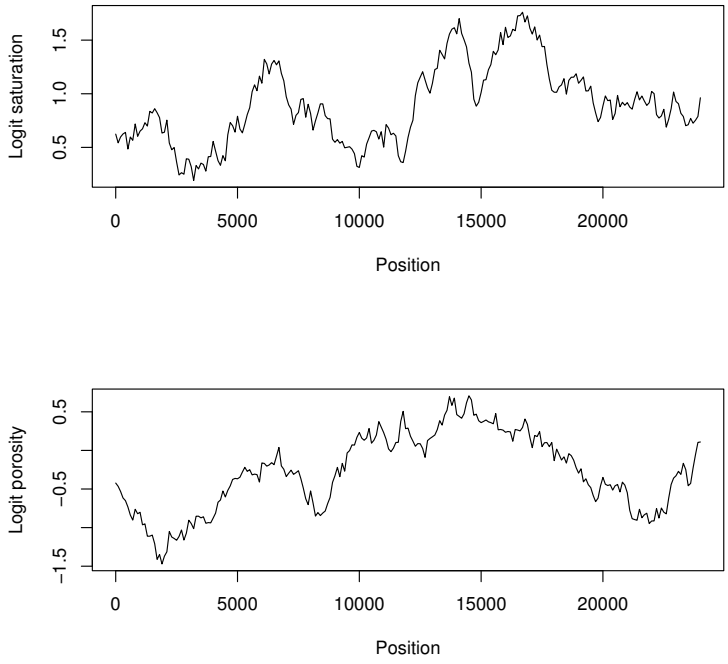

Figure 5.1: True logit values for the synthetic saturation and porosity. The values are a realization of $M \sim N(0, \Sigma_{synt})$

Archie		Gassmann	
C	1.28	K_0	38 Gpa
α	1.33	K_{water}	2.25 Gpa
β	0.14	K_{gas}	0.08 Gpa
Conductivity		Cap-rock properties	
ϑ_w	3.2 Ωm	V_P^C	2475 $\frac{m}{sec}$
ϑ_o	0.67 Ωm	V_P^s	1275 $\frac{m}{sec}$
		ρ^C	2500 $\frac{kg}{m^3}$

Table 5.1: Model parameters for both synthetic and real data.

zero. Using only seismic data to estimate ϕ also yields good results in this situation, but the accuracy is considerably increased when the information from the CSEM data is being taken into account. The saturation estimates gives a fairly precise image of the true values, but the variance is much larger here than for the porosity estimates. The estimates of s_w are also more spikey than the true solution, and they seem to be oscillating around the real values. This could be due to the lack of a smoothing parameter ξ in our prior model. The estimate of s_w based only on the seismic date misses the solution completely, and is very close to the a priori assumption $s_w = 0$. Figure 5.4 shows that outside the bounds of the seismic gather, all information about porosity is lost, while the saturation estimate still follows the true values closely, although with a substantial increase in variance. The estimates of σ_C^2 and σ_S^2 are shown in Figure 5.5. The Markov chain seems to converge almost immediately, and the mean values of σ_C^2 and σ_S^2 are small, although not zero. For all practical purposes however, noise levels of this magnitude are equal to zero noise.

We now add some noise to our data to see how the inversion estimates are affected. Figure 5.6 and 5.7 shows the estimates for s_w and ϕ when $\sigma_C^2 = 0.3$ and $\sigma_S^2 = 0.3$. For both s_w and ϕ the expected value of the posterior distribution still coincides closely with the true values, but the confidence intervals have broadened considerably for both parameters. Another thing worth noting is the variance of the saturation estimate in Figure 5.7. Outside of the dotted lines we have no seismic data, but this does not seem to affect neither the precision nor the variance in the saturation. This is in contrast to the zero noise case in Figure 5.4, where the variance increased significantly without seismic information. This indicates that information about saturation contained in the seismic data is easily lost when noise is added. In Figure 5.8 we see that our Gibbs sampler converges almost immediately. The posterior distributions for σ_C^2 and σ_S^2 have expected values 0.31 and 0.24 respectively.

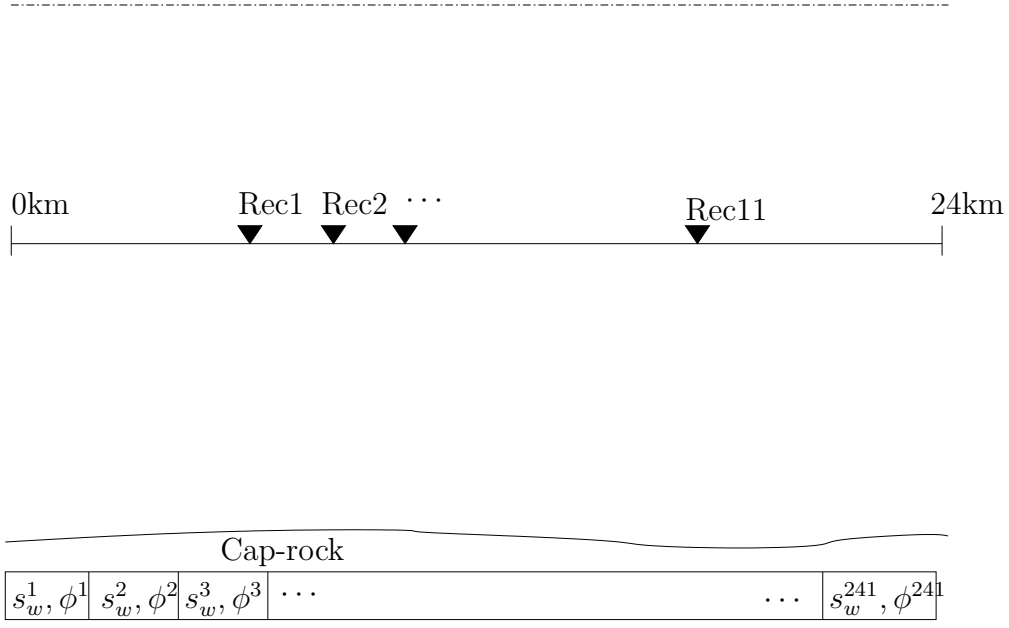

Figure 5.2: Synthetic data for porosity and saturation

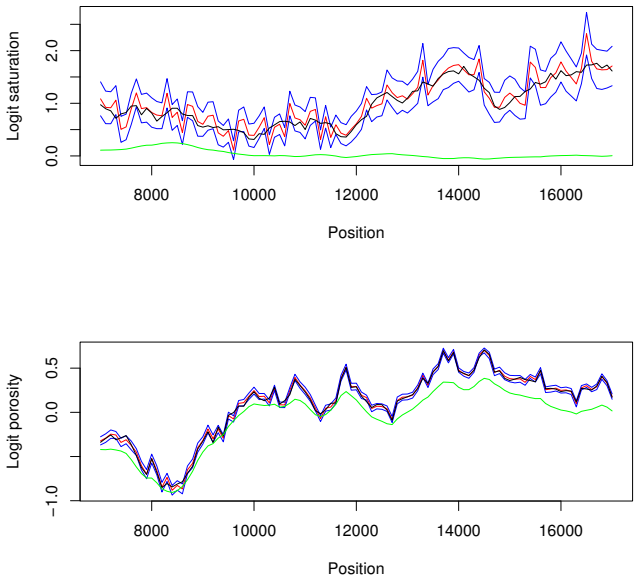

Figure 5.3: $\sigma_C^2 = 0$ and $\sigma_S^2 = 0$. No noise has been added to the data. The black lines show the true values, and the red lines are the estimated values. The blue lines are 95% confidence bounds, and the green line shows estimates based only on seismic data.

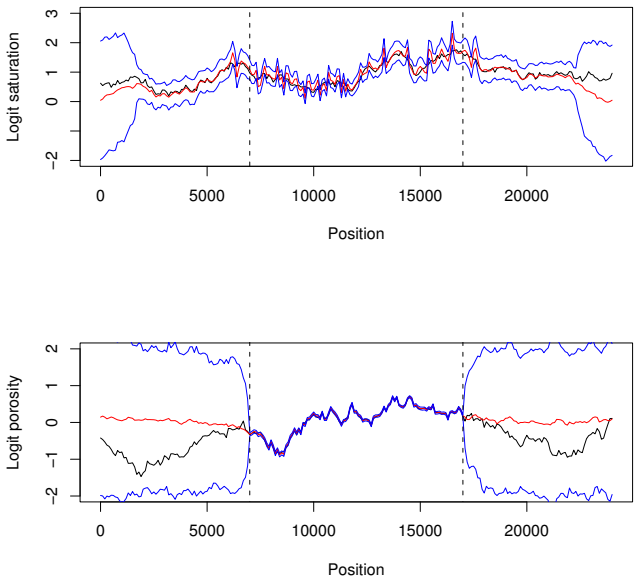

Figure 5.4: This is the same situation as in Figure 5.3 only with a broader perspective. Just outside the dotted lines we only have CSEM data, and to the far left and right we have no information at all.

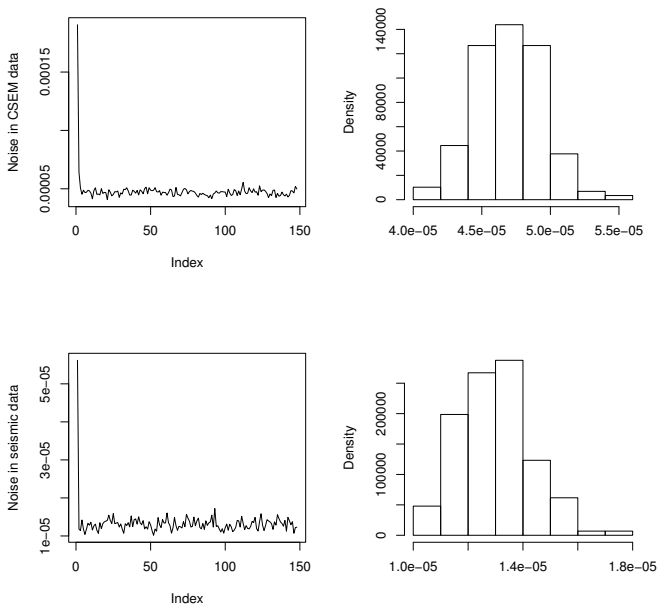

Figure 5.5: Convergence plot and posterior distributions for σ_C^2 and σ_S^2. The true value for both of them is zero.

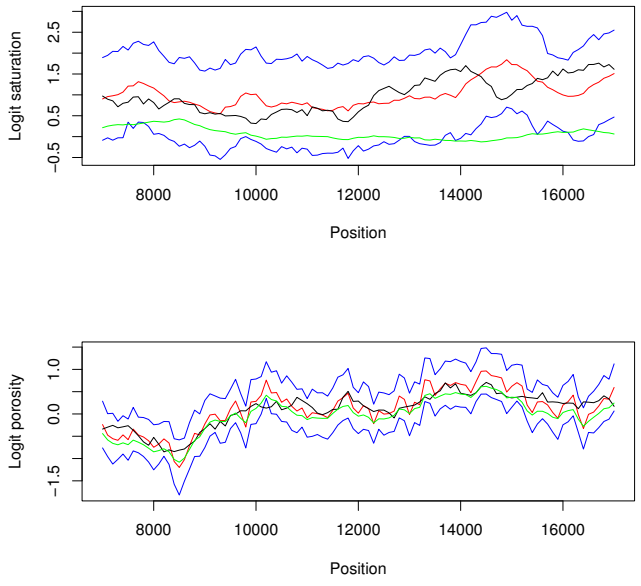

Figure 5.6: $\sigma_C^2 = 0.3$ and $\sigma_S^2 = 0.3$. The black lines show the true values and the red lines estimates from the joint inversion, with 95% confidence bounds in blue. The results from seismic data only rea showed in green.

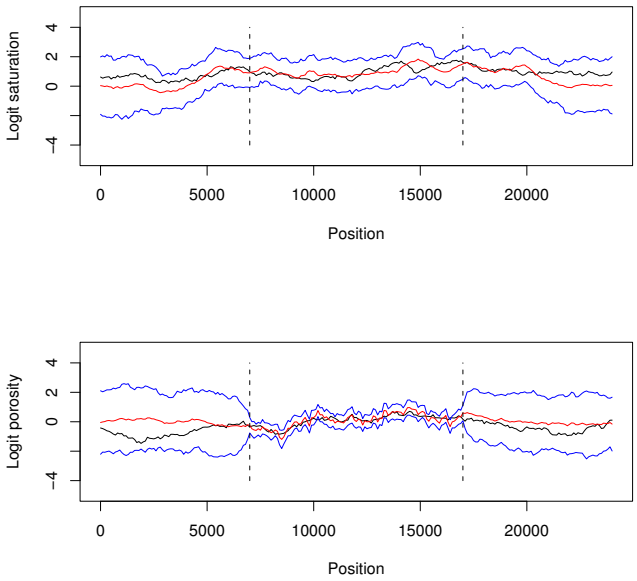

Figure 5.7: This is the same situation as in Figure 5.6 only with a broader perspective. Just outside the dotted lines we only have CSEM data, and to the far left and right we have no information at all

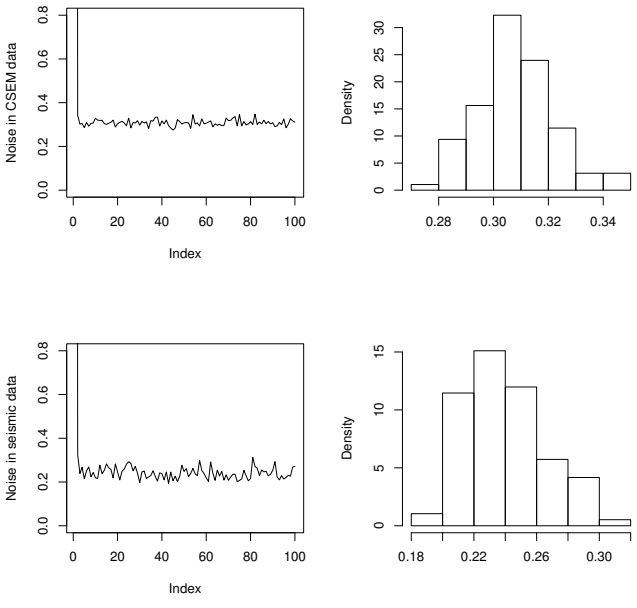

Figure 5.8: Convergence plot and posterior distributions for σ_C^2 and σ_S^2. The true value for both of them is 0.3

From the previous examples it would seem like the seismic data are the main contributor to information about porosity, while the CSEM data are mostly affected by the saturation exponent. To test this we have performed two additional runs of our inversion algorithm, one where $(\sigma_C^2, \sigma_S^2) = (0, 2)$ and one where $(\sigma_C^2, \sigma_S^2) = (2, 0)$.

Figures 5.9-5.11 shows the outcome of the simulation with $(\sigma_C^2, \sigma_S^2) = (0, 2)$. The estimate of s_w is almost identical to the estimate from the zero noise case shown in Figure 5.3, while the porosity estimate is much more inaccurate, and with a large variance. It is also worth noting the the porosity estimate from the joint inversion, and the estimate based solely on seismics are almost identical, in contrast to the zero noise situation, where porosity estimates from the joint inversion were better. This indicates that even though the CSEM data carries some information about the porosity, its impact is completely overridden by the noise-filled seismic data. The seismic estimate of the saturation is actually better here than ever before. This is most likely pure coincidence, and two other estimations with similar noise levels did not give saturation estimates nearly as accurate as here. The plots for σ_C^2 and σ_S^2 in Figure 5.11 indicate that they both converge almost immediately. The estimate of σ_C^2 stabilizes at $4.3 \cdot 10^{-5}$ which is as close to the true value of as we can hope to get. The seismic variance is, however, a bit undrestimated. σ_S^2 stabilizes at around 1.3, while the true value is 2. This might be due to the discrepancy between how the data are generated and our prior covariance matrix. Also, a σ_S^2 value of 2 equals an enormous amount of noise, which may cause some instability in the inverson.

In Figures 5.12-5.14, noise has been added to the CSEM data, while the seismic data are exact. Here we see the complete opposite of what happened in 5.9, the estimate of ϕ is very accurate, while the estimate of s_w has a large variance. This further strenghtens our initial assumption that the seismic data depends mostly on porosity, while the CSEM data depends on saturation. However, in figure 5.13 we see the the confidence bounds increases when we get outside the range of the seismic data. This indicates the when the seismic noise is low, some information about saturation can be extracted from seismic gathers. This was also seen in the example with zero noise, specifically in Figure 5.4. Figure 5.14 displays plots of the variances, and both σ_C^2 and σ_S^2 have been fairly accurately estimated. Correctly pinpointing the size of the CSEM noise causes the expected value of s_w to be very close to the true value even though the confidence bounds are rather wide. The large amount of noise also produces a smoother estimate than in previous simulations, which is more in line with the nature of the true values.

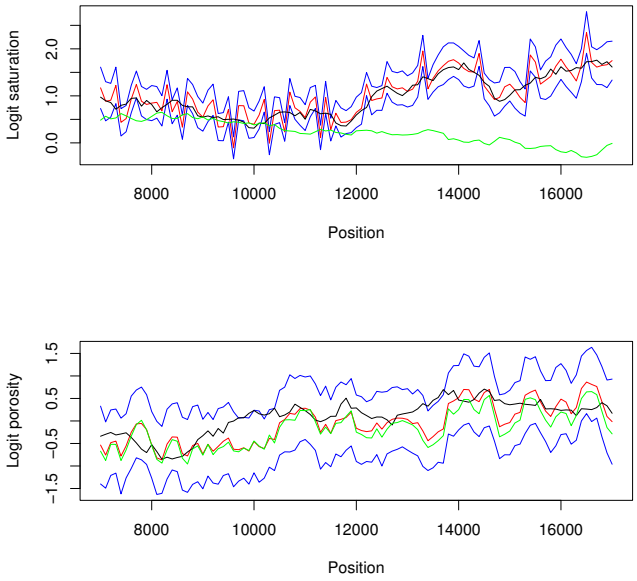

Figure 5.9: $\sigma_C^2 = 0$ and $\sigma_S^2 = 2$. Noise in the seismic data, but not in the CSEM data. The porosity estimate from the joint iversion is almost identical the estimate obtained from seismics only.

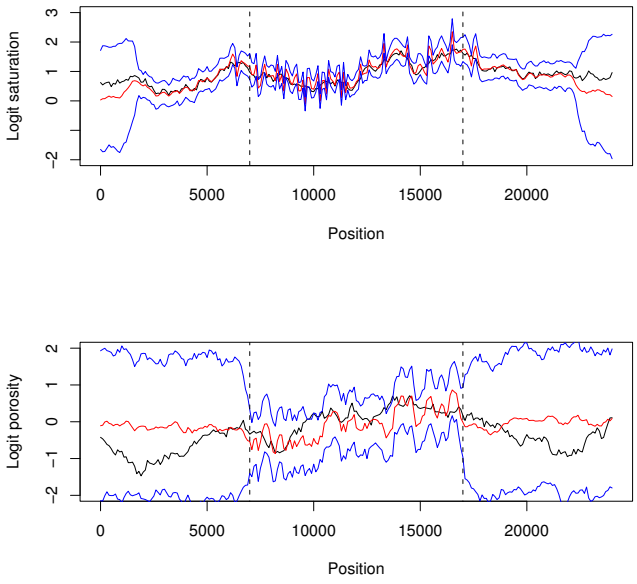

Figure 5.10: $\sigma_C^2 = 0$ and $\sigma_S^2 = 2$. Outside of the dotted lines the large value for σ_S^2 has no effect, as no seismic data has been gathered in this area.

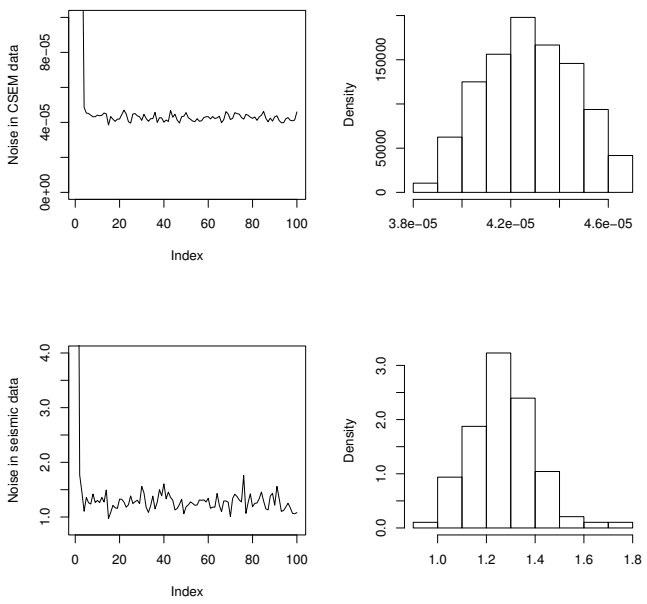

Figure 5.11: $\sigma_C^2 = 0$ and $\sigma_S^2 = 2$. The posterior distribution of σ_S^2 seems to be too far left, with a mean value of approximately 1.3. σ_C^2 behaves as expected.

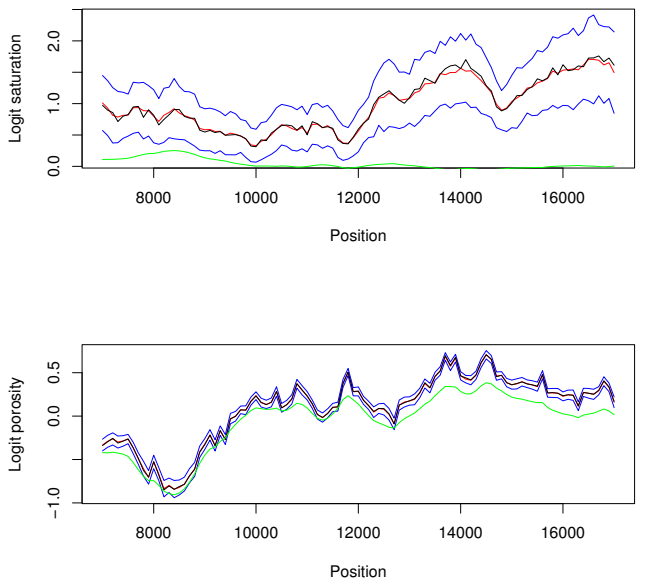

Figure 5.12: $\sigma_C^2 = 2$ and $\sigma_S^2 = 0$. Noise in the CSEM data, but not in the seismic data gives us an accurate estimate of the porosity. The saturation estimate is also good, but the confidence bounds are wide.

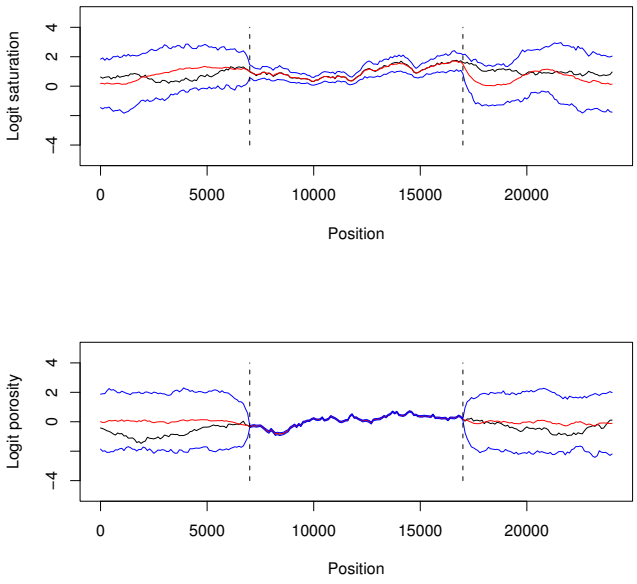

Figure 5.13: $\sigma_C^2 = 2$ and $\sigma_S^2 = 0$. The uncertainty in the saturation estimate expands considerably immediately outside of the seismic range.

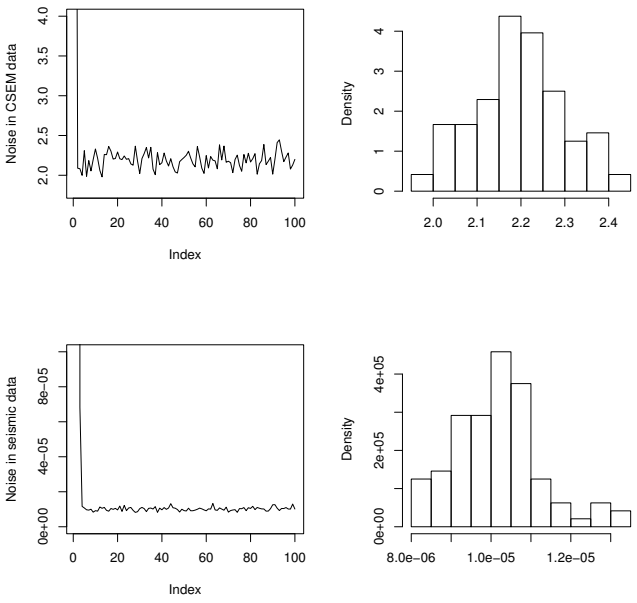

Figure 5.14: $\sigma_C^2 = 2$ and $\sigma_S^2 = 0$. Both parameters converges rapidly to values close to the true noise levels.

For all the simulations above, the prior covariance matrix has been fixed, with $\rho = 0.9$ and $\sigma_P^2 = 1$. These are the same numbers that were used when we generated the synthetic data and this may make our inversion algorithm appear more accurate than it is in reality. The reason for fixing the prior covariance matrix is that the Gibbs sampler will not converge to any meaningful values when no parameters have been set a priori. Instead it will tend to extreme solutions where one or more of the parameters increases indefinitely. It is, however, still of interest to find out how our prior assumptions affect the results, so in order to check our model's sensitivity to the prior covariance parameters, we have run 4 simulations where these parameters are either higher or lower than their real values. Table 5.2 summarizes the accuracy of the confidence bounds and size of standard deviations for these four simulations. $\bar{SD}$ is the mean size of the variance of the logit values for both s_w and ϕ, while Error is the amount of true values that lie outside our estimated 95% confidence bounds. Both $\bar{SD}$ and Error have been calculated based on estimations of logit-values horizontally located between 7000 meters and 17000 meters, i.e. in the area where we have both seismic and CSEM data.

In the middle of the table, numbers for a simulation with the correct prior values are displayed. The two simulations performing worst are the ones where $\sigma_P^2 = 0.5$. This is not surprising, because a low value for σ_P^2 indicates that we are fairly certain about the interval which the logit values lie within. Since this is not the case, we are imposing wrong information on our estimates, which in turn results in large standard deviations.

Setting $\sigma_P^2 = 2$, which is much higher than necessary, does not seem to have the same negative effect on our parameters, as this leaves most of the estimation up to the acquired data. In the simulation where $(\sigma_P^2, \rho) = (2, 0.3)$ the standard deviation is slightly larger than for the correct values, but this is most likely due to ρ being so low. Assigning ρ with too low a value means that we do not make full use of all the information we acquire, and this leads to higher uncertainty. This is also confirmed by the low Error in this simulation, which indicates that the confidence bounds should be narrower than our estimates. What is interesting to note is that for $(\sigma_P^2, \rho) = (2, 0.99)$ the results are better than when we use the correct parameters $(1, 0.9)$. The $\bar{SD}$ is significantly lower, and the Error is close to 5%. This is most likely due to the smoothing parameter ξ that was used in the generation of data, but not included in the prior. Raising the value of ρ counters the effect of not including ξ and gives a better description of the true situation.

$\sigma_P^2 \setminus \rho$	0.3	0.9	0.99
0.5	$\bar{SD} = 0.89$ Error$\simeq$1.5%		$\bar{SD} = 0.67$ Error$\simeq$3%
1		$\bar{SD} = 0.48$ Error$\simeq$2.5%	
2	$\bar{SD} = 0.54$ Error$\simeq$1%		$\bar{SD} = 0.32$ Error$\simeq$4%

Table 5.2: $\bar{SD}$ is the mean standard deviation in the area where we have both seismic and CSEM data. Error denotes the amount of values that lie outside of the 95% confidence bounds. Ideally this should be around 5%. $(\sigma_C^2, \sigma_S^2) = (1, 1)$ in all the simulations.

5.2 Troll data

The setup for collection of CSEM Troll data is very similar to that of the synthetic case discussed in the previous section. 24 receivers were placed on the seafloor in a straight line as illustrated in Figure 5.15. The sea-depth in this area is approximately 325 meters, and an electric dipole transmitter was lowered to 100meters, and towed along the line of the receivers, starting 10km southwest of receiver 1, and ending up 10km northeast of receiver 24. The transmitter emitted a signal for every fiftieth meter that was registered by the receivers within a range of 10km. So every receiver has registered signals from 10km southwest to 10km northeast of its position with 50 meter intervals, aproximately 400 signals per receiver. Unfortunately only 18 of the 24 receiver functioned as they were supposed to. Measurements were made for signals with frequencies of $0.25Hz, 0.75Hz$ and $1.25Hz$, but we will only focus on data from the $0.25Hz$ signal. The received CSEM data

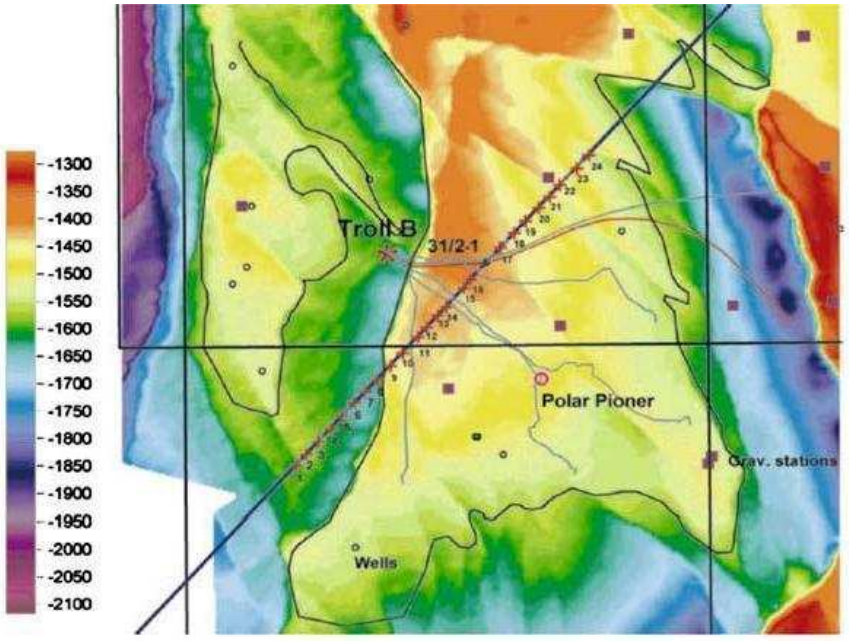

Figure 5.15: The figure indicates the location of the 24 CSEM receivers. Only 18 of the receivers functioned properly, and for receiver 3, 7, 10, 13, 17 and 21 no data were recorded. A seismic gather has also been performed in the same area, and we will be working with seismic data collected on the line segment between receiver 1 and receiver 24. The figure is from [18]

were not given on the same form that we have been working with and a data transformation was therefore necessary before applying the inversion method. This transformation is described in appendix A. Figure 5.16 shows the transformed data as a function of offset. For most of the receivers the recorded data are far from symmetrical for positive and negative offsets. This indicates rather large conductivity variations in the anomaly.

Figure 5.17 shows an image of the subsurface created from the full 2D seismic gather along the EM line. Our seismic model concentrates on transition between cap-rock and

anomaly, which is illustrated by a yellow line in the figure, and we will be working with seismic data picked along this line. Selection of these data are considered part of the pre-processing, and will not be further examined here, but it is worth noting that this is a difficult process which potentially introduces a lot of noise, especially because of the two large faults in the cap-rock. From the seismic data we find the depth of the anomaly, which is approximately 1200 meters below the seafloor. Figure 5.18 displays the values of R_{PP} and G_{AVO} picked along the yellow line in Figure 5.17.

The dimension of our datasets were $n_{ds} = 326$ and $n_{dc} = 1116$. For the seismic data we picked every third datapoint along the line between receiver 1 and 24, while for the CSEM data we only used data from offsets between 6.5km and 8km. When the offset becomes to small, the linear relation between offset and traveltime is no longer valid, while large offsets causes more noise in the data. The interval 6.5km-8km was chosen to balance these two considerations. The correlation coefficient ρ in our prior covariance matrix was set to 0.7. The other fixed model parameters were the same here as in the synthetic example. These are listed in table 5.1.

In Figure 5.19 and 5.20 we see the estimate of s_w and ϕ on the Troll site. The porosity estimate in Figure 5.20 confirms the results from the synthetic data. Outside the range of the seismic gather, all information about porosity is lost, and the estimate tends to its a priori expectation, which is 0. In the area where we do have seismic data, the logit values of the porosity ranges between 0.5 and 4. This corresponds to porosities between 0.29 and 0.11. The lowest porosity is found between 13.5km and 17km. This corresponds with the dark area in Figure 5.17. One would not expect this area to have such a low porosity, since a large part of the gas reservoir is located here. One explanation might be that the seismic data for this area are recording of the transition between the overburden and the cap-rock, and not between the cap-rock and the anomaly. This might be the case due to the prominent cap-rock feature seen in 5.17, and we have thus estimated the porosity in the cap-rock, and not the anomaly.

It is difficult to draw any clear conclusions about the gas reservoir from the saturation plot. Remember that to the far left and far right we have no data and the estimates therefore tends to the a priori values. Hence results earlier than 3km and after 27km might not be trusted. Figure 5.22 shows the saturation and porosity estimates, and also indicate the true gas saturated areas, while Figure 5.23 displays the true situation at the Troll field. Some features of the true situation are recognized in the saturation plot in Figure 5.22. The saturation has a spike between 22km and 24km which corresponds to low gas saturation in precisely this ares. Also, the genally low saturation values between 13km and 22km corresponds well with the true situation. However, the spike between 16km-17km and the low saturation values between 5km and 8km can not be related to any features seen in Figure 5.23.

Figure 5.21 shows convergence plots and histograms for σ_C^2 and σ_S^2. While they both stabilize almost immediately, the estimated level of the seismic variance is very high. Combined with the tendency to underestimate the seismic variance experienced in the synthetic case, we are left with seismic data with a lot of noise. σ_S^2 was multiplied with the a priori known seismic covariance matrix in 4.18. Setting $\sigma_S^2 = 9$ gives us a 95%

confidence interval for R_{PP} of magnitude 0.6 and 2.0 for G_{AVO}. In Figure 5.18 we see that typical values for R_{PP} are in the interval [-0.1,0.3] and for G_{AVO} [-0.4,0.4]. Thus the estimated noise levels indicate that a lot of the infomation in the seismic data are drowned in noise. σ_C^2 has a mean of approximately 0.42 which gives confidence intervals of magnitude 2.5. The size of the CSEM data ranges between [3,5] for appropriate offsets, and while the noise is still considerable, it is significantly less than in the seismic data.

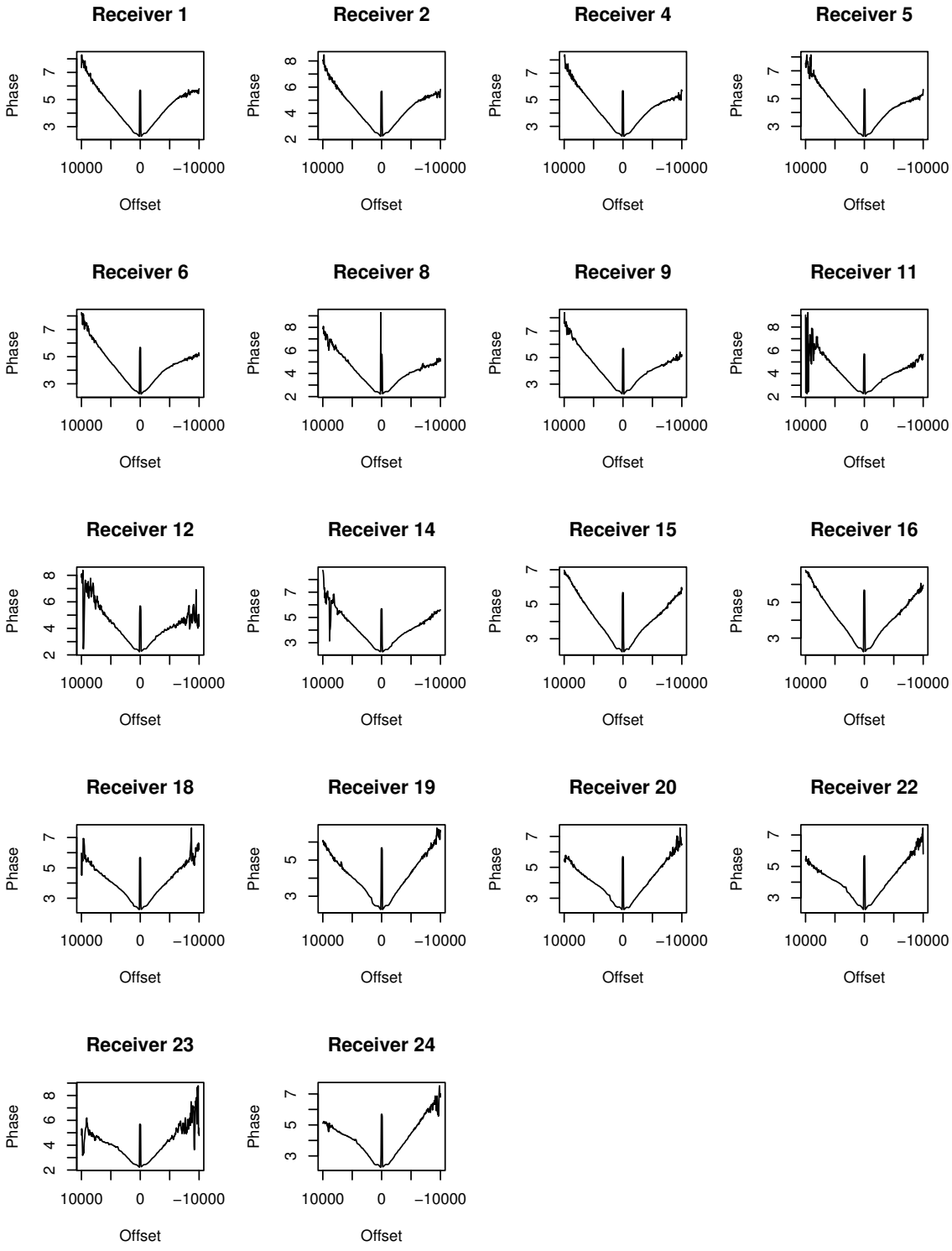

Figure 5.16: Phase as a function of offset for the 18 receivers used in the Troll CSEM gather.

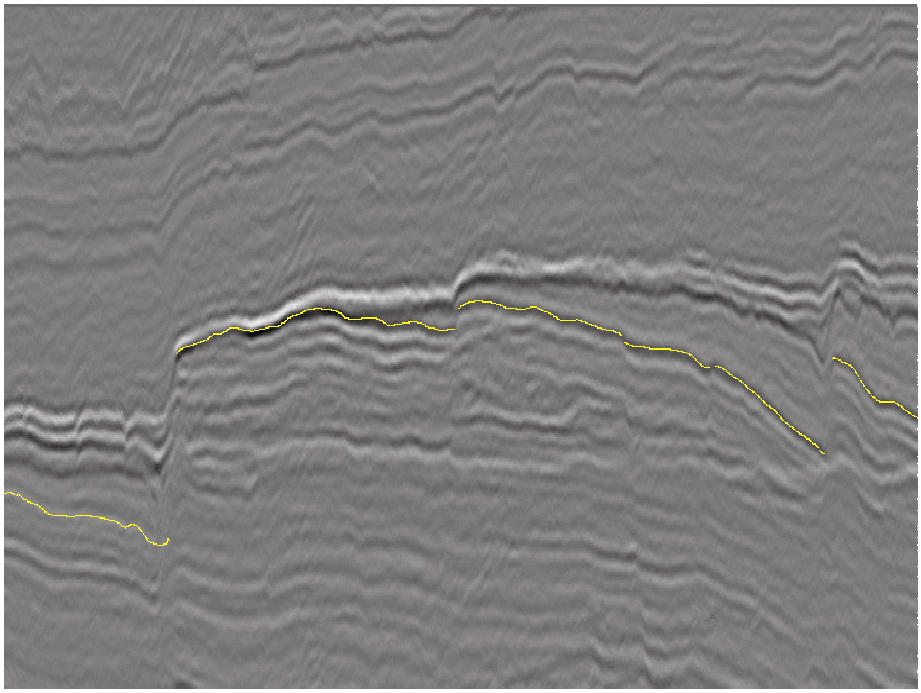

Figure 5.17: Image of the subsurface based on seismic date. A yellow line is drawn along the cap-rock/anomaly transition. The discontinuities in the line indicate faults.

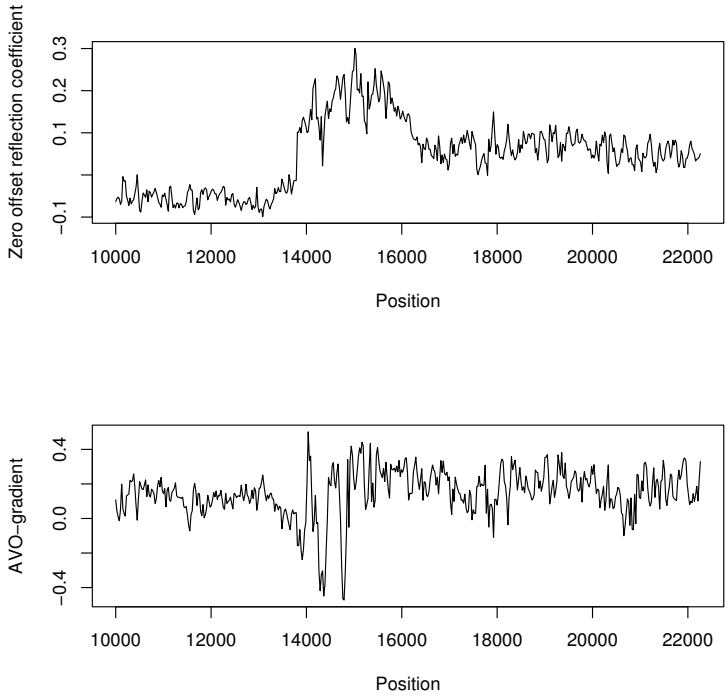

Figure 5.18: Values for R_{PP} and G_{AVO} picked along the yellow line in Figure 5.17.

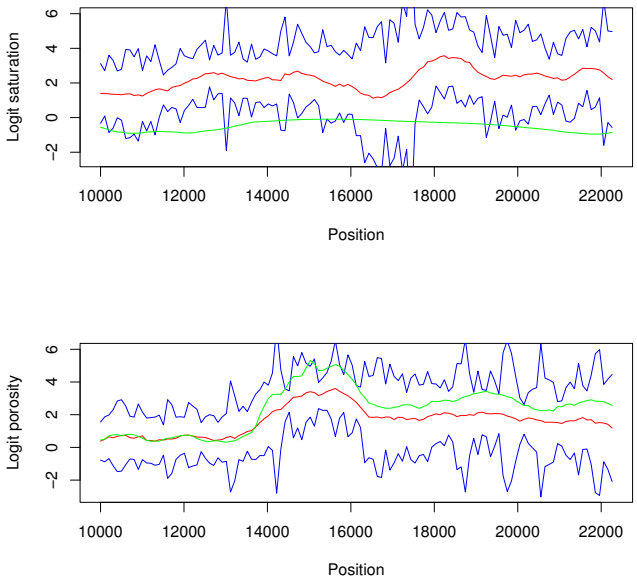

Figure 5.19: Estimates of logit values for water saturation and porosity at the Troll field. The red lines are the expected values, and the blue lines are the 95% confidence bounds. Estimates based solely on seismics are shown in green.

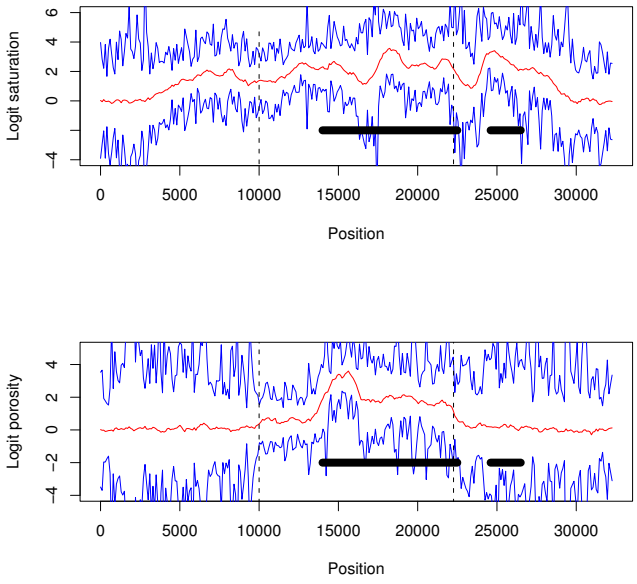

Figure 5.20: Logit values for saturation and porosity over the entire exploration area. The thick black lines marks the areas which are known to be gas saturated.

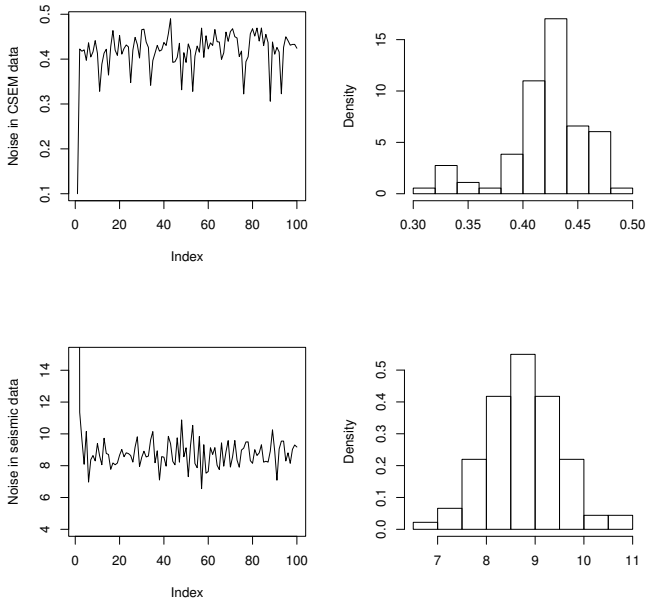

Figure 5.21: Histograms and convergence plots for σ_C^2 and σ_S^2 from the Troll data. Both parameters seem to converge rapidly. The expected value for $\sigma_C^2 = 0.42$ and for $\sigma_S^2 = 9$

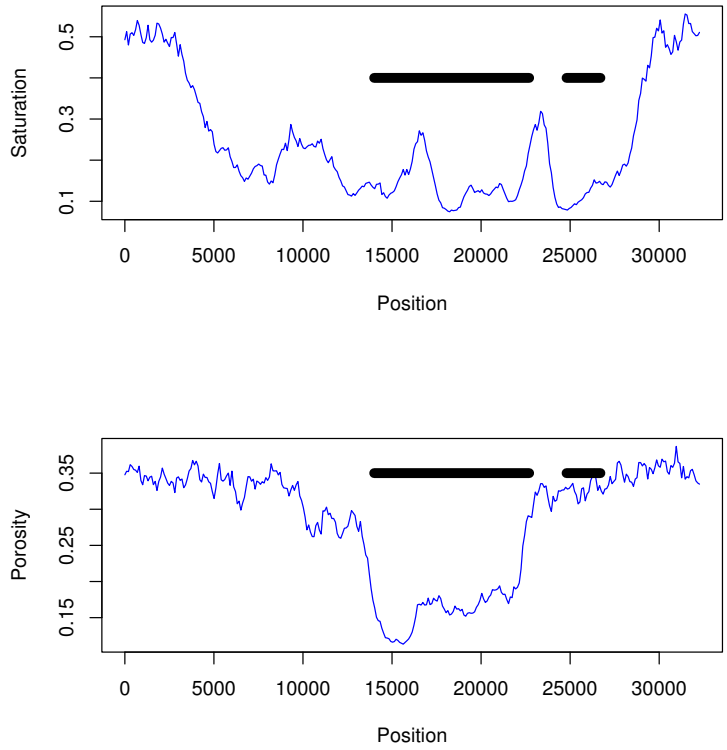

Figure 5.22: Saturation and porosity over the entire exploration area. The prior correlation coefficient $\rho = 0.7$. The thick black lines indicate gas saturated areas.

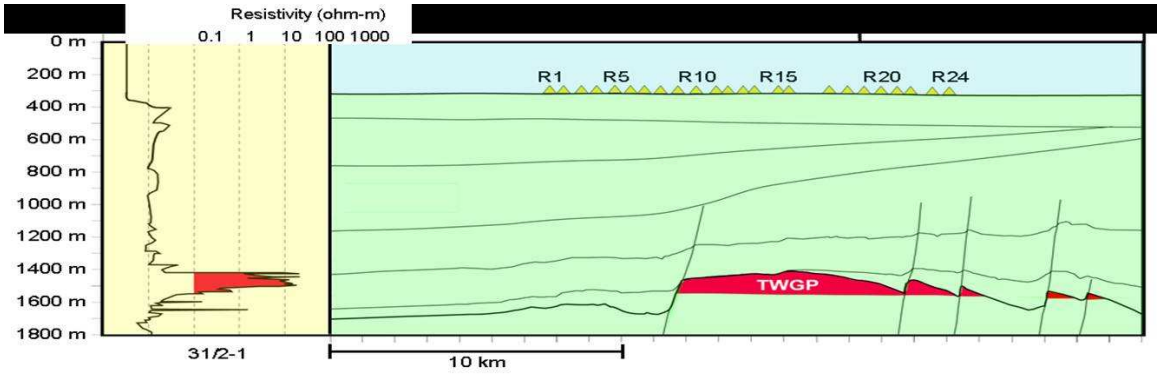

Figure 5.23: Actual situation at the Troll gas field. The main gas reservoir begins at around 14km and ends at 23km. There are also some gas concentrations between 25km and 27km. The figure is from [18].

6 Conclusion and suggestions for further work

In this paper we have studied the estimation of water saturation and porosity in the subsurface based on measurements of seismic and CSEM signals. An inversion method has been developed based on Bayesian statistics, and this method has been tested on a synthetic dataset where the true values were known, and a real dataset from the Troll field outside of Bergen. Both empirical and analytical relations have been utilized to link the observed data to s_w and ϕ. For the seismic data this involved Gassmann's and Zoeppritz' equations. The elastic constants used in Zoeppritz' equations were relatively insensitive to changes in s_w and when working on the synthetic dataset it proved difficult to get a reliable estimate of s_w based on seismic data. The porosity was, however, very accurately estimated by the seismic data, though the addition of CSEM lead to a slight increase in the precision. For the CSEM data we used Archie's law and ray-tracing to connect s_w and ϕ to traveltimes or phase. The constants in Archie's law were estimated from well logs, which gave us a very low porosity exponent. Because of this the CSEM data were mainly dependent on s_w, and the two data gathers complemented each other in regards to information about s_w and ϕ.

We have found that the parameters in both the prior- and the likelihood covariance matrix are crucial for the method's performance. Since estimation of all these parameters simultaneously leads to extreme solutions, we fixed the prior covariance using prior information about s_w and ϕ, and estimated two parameters in the likelihood covariance matrix utilizing a Gibbs sampler. In the synthetic case the noise in the CSEM data was accurately estimated for several different noise levels, while the parameter for the seismic variance was somewhat underestimated when the noise grew large.

The synthetic example showed a clear improvement in estimation accuracy when seismic and CSEM data where used in a joint inversion. This indicates that the theoretical foundation of the method is sound, and wothy of a more thorough analysis, For real data the results show some similarity with previous results from the Troll field, but not in all respects, and the uncertainty is large. There are many reasons for this possible misfit when applying our method on a real life situation. One of them being the large amount of error in the seismic data, which arises from difficulties in picking data along the cap-rock/anomaly transition. Also, we assume that the empirical relations, which have been calculated in one well, are correct outside of this well. This will not be completely accurate, and further increases the noise levels in our data. For the CSEM data it would be beneficial to implement a more realistic model for the CSEM signals behaviour in the overburden and anomaly, and to include all frequencies in the processed phase data. This would involve more complicated physics, but can be done without having to solve time-consuming diferential equation. A lot of deterministic work on this have been done in [14]. Another problem is that we are working in 1D and ignoring the two-dimensional lateral and vertical effects this simplification causes.

As mentioned in the introduction, previous works on this subject have focused on a vertical model where ϕ and s_w only varies with depth. A reliable 2D model combining variations horizontally and vertically would be a useful tool in the continuing search for offshore hydrocarbon reservoirs.

References

[1] K. Aki and P.G. Richards. *Quantitative seismology: Theory and methods*. W.H. Freeman and Co., 1980.

[2] L. Amundsen, L.O. Løseth, R. Mittet, S. Ellingsrud, and B. Ursin. Decomposition of electromagnetic fields into upgoing and downgoing components. *Geophysics*, 71:G211–G223, 2006.

[3] G.E. Archie. The electrical resistivity log as an aid in determining some reservoi characteristics. *Transactions of the American Institute of Mechanical Engineers*, 146:54–62, 1942.

[4] P. Avseth, T. Mukerij, and G. Mavko. *Quantitative seismic interpretation*. Cambridge, 2005.

[5] R. Bachrach. Joint estimation of porosity and saturation using stochastic rock-physics modeling. *Geophysics*, 71:O53–O63, 2006.

[6] J. Chen, G.M. Hoversten, D. Vasco, Y. Rubin, and Z. Hou. A bayesian model for gas saturation estimation using marine seismic AVA and CSEM data. *Geophysics*, 72:WA85–WA95, 2007.

[7] C.S. Cox, J.H. Filloux, and J. Larsen. Electromagnetic studies of ocean currents and electrical conductivity below the ocean floor. *The Sea*, 4:637–693, 1970.

[8] J. Eidsvik, P. Avseth, H. Omre, T. Mukejri, and G. Mavko. Stochastic reservoir characterization using prestack seismic data. *Geophysics*, 69:978–993, 2004.

[9] S. Ellingsrud, T. Eidesmo, M.C. Sinha, J.M. MacGregor, and S.C. Constable. Remote sensing of hydrocarbons layers by SeaBed logging (SBL): Results from a cruise offshore Angola. *Leading Edge*, 20:972–982, 2002.

[10] W.R Gilks, S Richardson, and D.J. Spiegelhalter. *Markov Chain Monte Carlo in practice*. Chapman and Hall, 1996.

[11] W.K. Hastings. Monte Carlo sampling methods using Markov chains and their applications. *Biometrika*, 57:97–109, 1970.

[12] Z. Hou, Y. Rubin, G.M. Hoversten, D. Vasco, and J. Chen. Reservoir-parameter identification using minimum relative entropy-based Bayesian inversion of seismic AVA and marine CSEM data. *Geophysics*, 70:O77–O88, 2006.

[13] G.M. Hoversten, F. Cassassuce, E. Gasprikova, G.A. Newman, J. Chen, Y. Rubin, Z. Hou, and D. Vasco. Direct reservoir parameter estimation using joint inversion of marine seismic AVA and CSEM data. *Geophysics*, 71:C1–C13, 2006.

[14] L.O. Løseth. Aymptotic evaluations of the marine CSEM field integrals. Submitted for publication to IEEE Transactions on Geoscience and Remote Sensing, 2007.

[15] L.O. Løseth, H.M. Pedersen, B. Ursin, L. Amundsen, and S. Ellingsrud. Low-freguency electromagnetic fields in applied geophysics: Waves or diffusion? *Geophysics*, 71:W29–W40, 2006.

[16] G. Mavko, T. Mukerij, and J. Dvorkin. *The Rock Physics Handbook*. Cambridge, 1998.

[17] A.G. Nekut. Electromagnetic ray-trace tomography. *Geophysics*, 59:371–377, 1994.

[18] T. Røsten, K. Hokstad, and B. Arnzen. 3-D depth migration operators for marine controlled-source electromagnetic data. SEG Technical Program Expanded Abstracts, 2006.

[19] J. Virieux, C. Flores-Luna, and D. Gibert. Asymptotic theory for diffusive electromagnetic imaging. *Geophys. J. Int.*, 119:857–868, 1994.

Appendices

A Phase scaling

The derivations in this appendix is largely based on [17]. An electric field E is given as

$$E = -i\omega\mu_0 I \frac{K_0(\gamma r)}{2\pi} \tag{A-1}$$

where ω is the angular frequency, I is a line current, r is the distance to I, K_0 is a modified Bessel function, $\gamma = (i\mu_0\omega\sigma)^{1/2}$ and σ is the conductivity. When $|\gamma r| \gg 1$ the Bessel function can be approximated to

$$K_0(\gamma r) \sim e^{-\gamma r}\sqrt{\frac{\pi}{2\gamma r}} \tag{A-2}$$

Inserting this into A-1 gives us

$$E \sim \frac{-i\mu_0\omega I}{2\pi}\sqrt{\frac{\pi}{2\gamma r}}e^{-\gamma r}. \tag{A-3}$$

From the CSEM experiment at the Troll-field we have measurements of the elctric fields amplitude α and the phase ξ.

$$\begin{aligned}
\alpha e^{\xi} &= E \\
\alpha e^{\xi} &= \frac{-i\mu_0\omega I}{2\pi}\sqrt{\frac{\pi}{2\gamma r}}e^{-\gamma r} \\
\xi &= -\frac{5\pi}{8} - r\sqrt{\frac{\mu_0\omega\sigma}{2}} \\
-r\sqrt{\mu_0\sigma} &= (\xi + \frac{5\pi}{8})\sqrt{\frac{2}{\omega}} \\
-\tau &= (\xi + \frac{5\pi}{8})\sqrt{\frac{2}{\omega}}.
\end{aligned} \tag{A-4}$$

Since we are only interested in the phase-shift from source to receiver we can ignore the sign. Hence our expression for the travel-time is

$$\tau = (\xi + \frac{5\pi}{8})\sqrt{\frac{2}{\omega}}. \tag{A-5}$$

List of Figures